

Initial saturation dynamics and current sheet formation of external kink modes in near circular tokamak and $l = 2$ stellarator geometry

R Ramasamy,¹ M Hoelzl,¹ S Henneberg,² E Strumberger,¹ K Lackner,¹ and S Günter¹

¹Max-Planck Institut für Plasmaphysik, Boltzmannstraße 2, 85748 Garching bei München, Germany

²Max-Planck Institut für Plasmaphysik, Wendelsteinstrasse 1, 17491 Greifswald, Germany

(*Electronic mail: rohan.ramasamy@ipp.mpg.de)

Equilibrium and initial value codes are used to study the initial saturation of external kinks in low β tokamaks and $l = 2$ stellarators. Within the defined parameter space, the saturated states observed with helicity preserving VMEC computations do not converge to a single solution with increasing spectral resolution. This is because the ideal MHD model allows for the unconstrained formation of current sheets at the plasma boundary. Helicity conservation, the incompressibility constraint, and magnitude of the induced plasma current spike are used to constrain the solution space towards a physical solution. Parameter scans of the edge safety factor, and external rotational transform show how the structure of a saturated $(4, 1)$ external kink depends on the magnetic geometry of classical stellarators. Saturated states can be identified at different field periodicities which decrease in amplitude with increasing external rotational transform, following the expected trend informed by the modification of the linear growth rate. For a subset of these perturbed equilibria, the magnetic energy spectrum is used to demonstrate that the nonlinear mode coupling of the perturbation is dominated by members of the toroidal mode family of the observed MHD instability. The nonlinear magnetic energy spectra, poloidal localisation of induced current sheets, and predicted redistribution of poloidal magnetic energy from the vacuum to plasma region are compared with JOEKE simulations to further explain observations from VMEC results. This work constitutes a first step towards using both approaches to analyse external modes in advanced stellarators.

I. INTRODUCTION

The magnetohydrodynamic (MHD) instabilities that occur in toroidally confined fusion plasmas can produce a significant degradation in confinement, and, in the worst case, lead to a disruption. While optimised stellarators are widely considered to be much more robust than tokamaks in this context, the β limits of stellarators¹, and the recently observed plasma terminating events in W7-X², are still not fully understood. As a result, there is a demand for nonlinear approaches to modelling MHD phenomena in non-axisymmetric devices.

Among such methods, the VMEC free-boundary code³ offers a computationally efficient solution to nonlinear MHD problems in the ideal MHD limit. Though VMEC and other equilibrium codes do not evolve the MHD equations dynamically, it has been proposed that perturbed equilibrium states can be found which correspond to the final state of a MHD perturbation. This is considered possible if the perturbed solution is appropriately constrained to have a physically meaningful link to the initially unperturbed equilibrium from which the dynamics evolve^{4,5}.

For ideal MHD perturbations, the typical constraint that is applied is the conservation of helicity. The approach has been used to study both dynamical problems where the perturbed state is driven using an external perturbation such as resonant magnetic perturbations (RMPs)^{6,7}, as well as to study nonlinearly saturated ideal MHD equilibrium states in a variety of tokamak scenarios^{8–12}. For the latter case, both internal, and external ideal MHD modes have been modelled, and validated against other linear, and nonlinear MHD approaches^{13,14}.

This technique has also been applied to the modelling of interchange modes in a Helias configuration¹⁵. The periodicity breaking modes were found to lead to much milder edge dis-

tortions than those observed in similar tokamak studies, even at high plasma β – the ratio of plasma and magnetic pressure. Though these results did not conserve helicity, or enforce physical constraints that link the unperturbed equilibria and saturated states explicitly, they have motivated discussion regarding the use of equilibrium codes to understand nonlinear MHD phenomena in stellarators. Of particular interest to the authors is the application of this approach to study external modes in QA configurations. The saturated MHD states found in VMEC would be a valuable starting point for transport calculations to see the negative influence such modes could have on confinement. The perturbed equilibria could also provide a nonlinear benchmark for the recent non-axisymmetric extensions of nonlinear MHD codes^{16,17}.

Other than the interchange modes that have been modelled in a Helias reactor, and the modelling of fixed boundary internal instabilities in a quasi-axisymmetric (QA) device using NSTAB¹⁸, the authors know of no other studies that have used the ideal MHD equilibrium approach to understand nonlinearly saturated MHD modes in stellarators. In this paper, nonlinearly perturbed states are computed for simple tokamaks, and $l = 2$ stellarators with two and five fold periodicity. While these devices are much simpler than the optimised configurations that are of interest to the fusion research community at the moment, they provide a reasonable test bed for understanding the methods involved in this approach, such that the structure of perturbed MHD states in stellarators can be analysed in detail. Such equilibria can also be used to understand how the saturated amplitude, and the nonlinear mode structure of ideal MHD instabilities varies as a function of the applied external rotational transform and field periodicity, denoted by t_{ext} and N_p , respectively. This is one of the main questions that is considered herein.

In the initial work towards this goal, several unexpected features were found in the results. Within the considered parameter space, the saturated perturbation amplitude was found to not converge with increasing spectral resolution, growing to an arbitrary size. Similar observations of poor numerical convergence have been made in the appendix of Ref. 19. Studies that have reported better convergence results are often fixed boundary, enforcing a stronger constraint on the perturbation amplitude²⁰. Further, when comparing results at different spectral resolutions, the physical trends in the nonlinear perturbation amplitude were found to differ. As such, an important question arises – which nonlinearly saturated state is the most physically meaningful? A detailed analysis of the features of such perturbed VMEC equilibria has been undertaken to provide an answer to this question.

In this subsequent analysis, features of the nonlinear magnetic energy spectra, and spatial distribution of the current sheets have been analysed and compared with JOEKE – an initial value problem solver, which can evolve the viscoresistive MHD equations dynamically²¹. This code has recently been extended to model stellarators²², and offers an alternative path towards interrogating their nonlinear MHD stability properties, using a very different set of numerical methods from the equilibrium approach.

Free boundary tokamak simulations, and preliminary fixed boundary stellarator simulations are used to further understand the nonlinear observations from VMEC. Three particular observations are targeted. First, helicity preserving VMEC computations often show an increase in the total potential energy over the integrated plasma volume. This unintuitive result is shown to be due to an exchange of energy between the plasma and vacuum region, excluded from the integration domain in VMEC. Secondly, the negative current sheets which form at the plasma boundary in VMEC are shown to be very sensitive to numerical parameters. By comparing with the current sheets in JOEKE, the correct structure of the sheets can be identified. Lastly, nonlinear stellarator simulations are used to support the conclusion that the perturbed magnetic energy does decrease as a result of increasing t_{ext} .

The results are continued far enough into the nonlinear phase to demonstrate that disruptive internal dynamics could be present, which cannot be captured by the ideal MHD model implemented in VMEC. While differences are observed in the two codes, the authors would argue that the deviations are actually rather small given the significant difference in the numerical methods used, and that the comparison of the two methods has helped to corroborate a story of how the initial kink dynamics in such geometries unfolds.

The remainder of this paper is outlined as follows. The method for finding nonlinearly perturbed states in VMEC, and the parameter space in which free boundary perturbed VMEC equilibria are computed is discussed in Section II. The resolution requirements are studied, identifying that current sheets form at the plasma boundary with increasing radial resolution, and that the computed perturbed state can depend on the poloidal and toroidal resolution of the computation. This result is consistent with previous studies that conclude the saturation of an ideal kink instability requires some localised re-

sistivity to prevent current sheets from growing indefinitely large²³.

These numerical convergence properties introduce a challenge for resolving the saturated mode. The second observation implies that the saturated MHD perturbation is not well defined by enforcing helicity conservation alone. As a result, further constraints, or an intuition about the mode structure are necessary to determine a physically meaningful solution. In this study, incompressibility, which is an expected condition for high aspect ratio external kink modes²⁴, and the increase in toroidal plasma current — the I_p spike — from the unperturbed to perturbed equilibrium are used to identify the resolution parameters which lead to the most physically meaningful saturated mode. These indicators are used *a posteriori*, after the VMEC computations are converged, to filter through the solution space in VMEC, rather than modifying the convergence algorithm within the code itself.

In Section III, the behaviour of the nonlinearly saturated mode structure on the q profile and external rotational transform is evaluated. The nonlinear perturbation amplitude in general follows the linear growth rate of the initial ideal MHD instability as expected. However, deviations are observed in some solutions which are thought to be alternative bifurcated states of the equilibrium. The nonlinear magnetic energy spectrum is then considered in Section IV, to show that the stellarator perturbations are dominated by the toroidal harmonics that are within the toroidal mode family of the instability, rather than the nearest neighbours of the dominant $n = 1$ mode, as in the tokamak case. In addition, it is shown that the $n = 0$ magnetic energy inside the simulation domain increases, despite being the dominant contributor to the instability.

The observations from VMEC computations are then compared with JOEKE tokamak and stellarator simulations in Section V. Analysis is carried out to understand the increase of the $n = 0$ component of the poloidal magnetic energy, the poloidal localisation of current sheets at the plasma boundary, and whether an increase in t_{ext} reduces the perturbed mode amplitude. The paper is then concluded with an outlook for future work on advanced stellarators in Section VI.

II. COMPUTATION OF PERTURBED FREE BOUNDARY VMEC EQUILIBRIA

The algorithm implemented in VMEC is well documented in Ref. 25, and the methods applied in this paper follow the approach of previous studies, which have used VMEC to compute nonlinearly perturbed equilibrium states^{10,12}. A brief review of this approach follows in this Section.

The ideal MHD potential energy, W_{mhd} , can be written as

$$W_{\text{mhd}} = \int \frac{B^2}{2\mu_0} + \frac{p}{\gamma - 1} dV. \quad (1)$$

where B is the magnetic field strength, p is the plasma pressure, and μ_0 and γ are the vacuum magnetic permeability, and heat capacity ratio, respectively. VMEC minimises W_{mhd} of

the plasma and vacuum region up to a prescribed level of accuracy in the ideal MHD force balance equation

$$\mathbf{j} \times \mathbf{B} - \nabla p = 0, \quad (2)$$

where \mathbf{j} , \mathbf{B} and p are the current, magnetic field and plasma pressure, respectively.

For MHD unstable equilibria, it is possible for the convergence algorithm to find a nonlinearly perturbed state. This makes sense as the MHD energy can be further minimised by physical MHD perturbations if the initially targeted equilibrium is ideal MHD unstable. The force imbalance produced by the instability can eventually fall if the drive for the MHD instability reduces with the growth in the perturbation. In this case, the equilibrium will converge to a new equilibrium, which is physically interpreted as a nonlinearly saturated MHD instability. This type of convergence behaviour is shown using the force residual in VMEC in Section II A.

It is challenging to construct MHD equilibria that will saturate nonlinearly in VMEC. This is because perturbed states can only be found by converging the equilibrium to force residuals that are well below the tolerances necessary for normal equilibrium studies. In this study, the tolerance in the force residuals for convergence, f_{tol} , is set to be less than 1×10^{-16} . In the authors' experience, large scale MHD structures typically observed in low (m, n) modes can be difficult to converge. Equally, small scale, high (m, n) modes require a large number of Fourier harmonics to converge and thus are similarly challenging to find. Medium scale perturbations between $m=4$ and $m=6$ can be converged for $n = 1$ when considering external kink instabilities. Typically $n > 1$ perturbed states have only been observed in the literature for RMP cases^{6,26}, where the state is externally driven, and thus easier to find.

To study external modes using VMEC, the plasma boundary must be allowed to deform. This requires a free boundary solution to the MHD equilibrium, which in turn requires a representation of the externally generated vacuum magnetic field. The virtual casing principle²⁷, which has been implemented in EXTENDER²⁸, can be used together with the NESCOIL²⁹ and MAKEGRID codes to generate an appropriate vacuum field.

The advantage of this approach is that a vacuum magnetic field can be calculated which recovers the plasma shape of interest more accurately than using a description of a real set of coils. Scans of different parameter dependencies can be conducted without the painstaking task of modifying the coil currents to get the desired plasma shape, by re-calculating the vacuum field from an initial fixed boundary equilibrium calculation. The disadvantage is that the vacuum field used does not represent the coil system used for a real device. Because this paper is not concerned with a particular experiment, and focuses on the general parameter dependencies of the saturated free boundary modes, the virtual casing principle is considered appropriate.

As mentioned in Section I, helicity conservation is an appropriate constraint for studying ideal MHD perturbations. For this reason, the equilibria studied in this paper have been

computed fixing the ι profile during the computation, as this enforces that the helicity of the plasma is conserved^{4,14}. Finding perturbed states that constrain ι instead of the toroidal current j can be more challenging, but is necessary to ensure a physical link between the unperturbed and nonlinearly saturated equilibrium state.

A. VMEC convergence behaviour

The different convergence behaviours of the VMEC force residuals that have been observed in this study are shown in Figure 1. Only the radial force residual, F_R , as defined in Ref. 25, is shown. All residuals computed by VMEC are observed to have the same behaviour in a given computation. Figure 1 (a) shows an equilibrium that converges successfully to an unperturbed solution. In this unperturbed case, the force residual decreases monotonically, as is expected with the minimisation of the W_{mhd} energy. For the perturbed cases in Figure 1 (b) and (c), it can be seen that the force residuals increase, as the instability is found and the force balance of the equilibrium is lost. Note that this often occurs at a relatively low residual value, below 10^{-13} , which would normally be considered reasonably converged in equilibrium studies. If a new perturbed state is found, the residuals must fall as the new perturbed state is reached, leading to the behaviour in Figure 1 (b). Similar observations of the force residual have been observed in studies of magnetic island formation using NSTAB¹⁸.

In many cases however, the force residuals continue to rise, until the VMEC algorithm detects the unfavourable behaviour. The equilibrium is then reset to an earlier stage, and the numerical time step parameter is decreased in an attempt to improve convergence. Often the smaller numerical time step does not lead to a converged solution and the process repeats indefinitely. Though the residuals still remain relatively low compared to normal equilibrium studies, the results produced by these cases are either considered to be numerical instabilities, or real MHD instabilities that lead to such large perturbations that they can be considered disruptive. The perturbed states reported in this paper all have the convergence behaviour shown in Figure 1 (c).

B. Equilibria and scale invariance

In this study, simple tokamaks and classical $l = 2$ stellarators were targeted at $\beta \approx 0$. As a result, due to the scale invariance of ideal MHD, the behaviour of the saturated modes that are evaluated can be assumed to be a function of the magnetic geometry alone. This means that the parameter space at $\beta \approx 0$ is defined by the external rotational transform, ι_{ext} , and the safety factor profile, $q(s)$, where $q(s)$ is in turn dependent on $j(s)$ and the shaping of the plasma.

To simplify the parameter space further, the initial toroidal current density, $j(s)$, of the considered equilibria is prescribed to have an Ohmic profile, similar to the analytic studies by Wesson³⁰

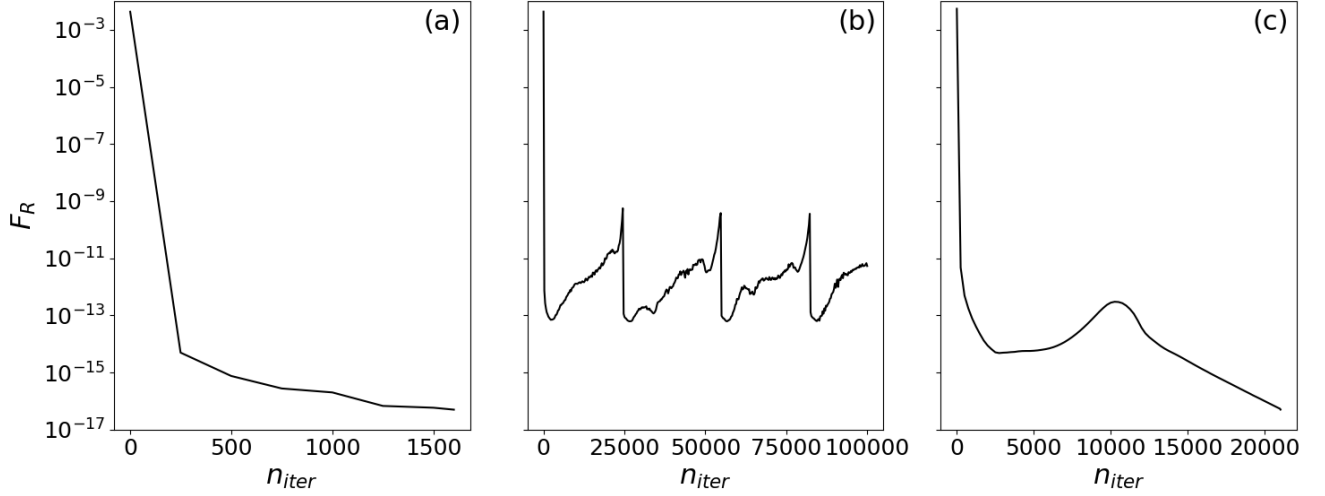


FIG. 1. Plots of the force balance residuals for VMEC computations during the convergence. An unperturbed case (a) and perturbed cases with poor (b) and good (c) convergence are shown.

$$j(s) = 1 - s^p, \quad (3)$$

where s is the normalised toroidal flux, $\hat{\Phi}$, and p is a constant.

All equilibria considered have a high aspect ratio, $A = a/R_0 = 0.1$, where a is the minor radius along the midplane, and R_0 is the major radius of the plasma axis. In order to determine a parameter space for finding nonlinearly perturbed states, tokamak cases were first considered, using $p = 2 - 4$. The elongation, $\kappa = b/a$, where b is the maximum height of the toroidally averaged plasma boundary, defined by the $n = 0$ boundary coefficients, above the major axis, and edge safety factor, q_{edge} were also varied.

Saturated states with quartic current profiles were difficult to converge while constraining the q profile. Using cubic and quadratic profiles, saturated (4, 1) modes could be found. Figure 2 (a) shows the variation of the q profile with the plasma elongation for simulations with cubic current profiles, setting $q_{\text{edge}} = 3.85$. The saturated state could only be found in VMEC for $\kappa \geq 1.25$. For lower values approaching a circular plasma, the convergence behaviour in Figure 1 (c) was observed.

The normalised growth rate of the (4, 1) external kink mode, $\hat{\gamma}_{41} = \gamma/\tau_A$, can be computed from the unperturbed equilibrium state using CASTOR3D³¹. The growth rate is normalised by the Alfvén time, $\tau_A = B/\sqrt{\mu_0 \rho}$, where ρ is the ion mass density. This accounts for variations in the magnetic field strength between equilibria. The growth rates are shown in Figure 2 (b). It can be seen that $\hat{\gamma}_{41}$ increases with decreasing κ . As such, it is thought that the poor convergence at low κ is due to the instability being too strong to reach a saturated state. Quadratic profiles were also computed, but again the saturated states did not converge well when decreasing κ . Scans with a higher q_{edge} , targeting a (5, 1) instability also failed to converge for plasmas with lower elongation. For

this reason, the (4, 1) external kink was targeted at $\kappa = 1.25$ for more detailed scans, varying the magnetic geometry by modifying $q(s)$ and l_{ext} .

C. Resolution scans

Before proceeding to scans of the physical parameters, q_{edge} and l_{ext} , it is important to understand the influence of resolution parameters on the perturbed equilibria that are being considered. In the following, resolution scans are carried out to help narrow the parameter space of numerical parameters used in exploring physical dependencies.

Analysis of global quantities

The $n = 1, m = 4$ Fourier component of the boundary displacement can be used as a metric for studying the behaviour of the mode with different numerical parameters. The Fourier decomposed, perpendicular plasma displacement, E_{\perp} , is computed in straight field line coordinates using a similar method to previous studies^{10,32}. An example of the Fourier decomposition of the normalised displacement is shown in Figure 3 for a stellarator case with $q_{\text{edge}} = 3.9$, $l_{\text{ext}} = 0.098$, and two fold periodicity. It can be seen that the Fourier displacement is dominated by the $n = 1, m = 4$ Fourier component. The poloidal and toroidal sidebands are below $\approx 10\%$ of the dominant mode, as expected for an instability in a low β , high aspect ratio $l = 2$ stellarator, where poloidal and toroidal mode coupling should be limited. As a result, the $n = 1, m = 4$ Fourier component alone, $E_{\perp, (n=1, m=4)}$, is used as a measure of the mode amplitude and its variation with resolution parameters.

In previous studies of RMPs³³, it was found that computations of tokamak plasmas did not converge to a single solu-

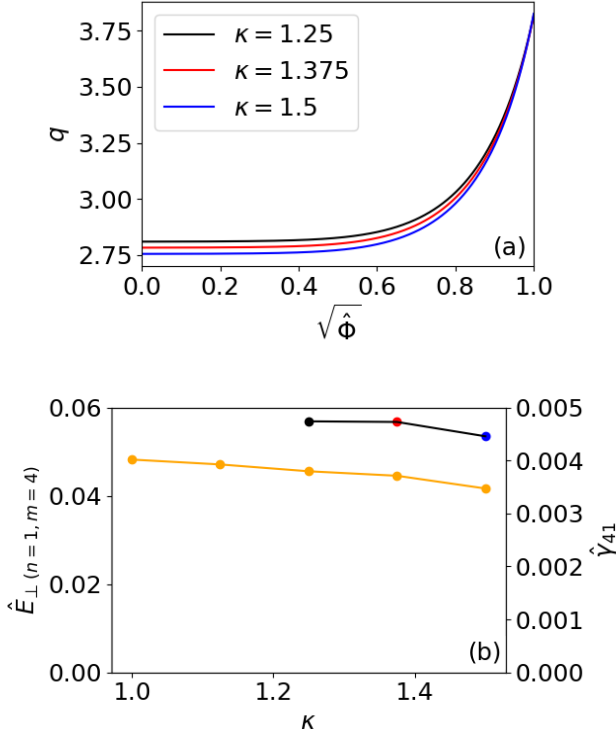


FIG. 2. Plots of q profile (a) and normalised displacement amplitude (b) of the saturated states found for $p = 3$, $q_{\text{edge}} = 3.85$, with varying κ . The displacement amplitude (b, black, left axis) is compared with the normalised growth rate (b, orange, right axis) computed with CASTOR3D. States were found only for $\kappa \geq 1.25$. Equilibria failed to converge well at lower elongations.

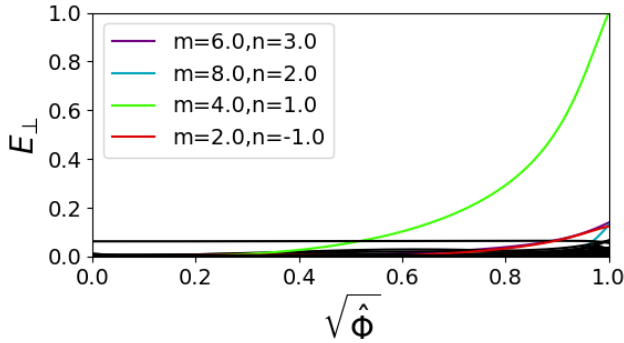


FIG. 3. Fourier decomposed nonlinearly perturbed displacement of the VMEC solution for a $l = 2$ stellarator with two fold periodicity and $t_{\text{ext}} = 0.098$.

tion with increasing spectral resolution. It was argued that this could be due to the high poloidal resolution required in order to resolve the resonant poloidal mode number at the edge. A similar observation has been made in this study, as shown in Figure 4 (a-c), which shows $\hat{E}_{\perp}(n=1, m=4)$ as a function of the radial, N_s , toroidal, n and poloidal, m , resolution. Results are

shown for a tokamak and $l = 2$ stellarators with $N_p = 2$ and 5 with $q_{\text{edge}} = 3.9$ and $t_{\text{ext}} \approx 0.1$ in the stellarator cases.

While the displacement of the plasma boundary is converged at reasonable radial resolutions, the poloidal resolution is not converged for any of the simulated cases. It should be noted that higher resolution simulations were attempted but were not tractable due to high computational cost, leading to convergence difficulties. The implied contributions to the saturated mode structure from the higher poloidal harmonics is plausible, given that $m = 4n$ modes are required to resolve the resonant poloidal mode of a given toroidal mode number. In order to confirm that the solution converges when the resonant harmonic is included, computations using $n = 3$ are shown in Figure 4 (c). It can be seen that at this lower toroidal resolution, the computation converges at approximately $m = 15$, soon after the resonant $m = 12$ mode is passed. It should be noted that the strong mode coupling observed in Figure 4 (c) is not seen in the representation of the normalised perturbed displacement $\hat{E}_{n=1, m=4}$, because this displacement is computed in straight field line coordinates, such that the mode coupling is accommodated in the choice of poloidal angle, $\theta^* = \theta + \lambda(s, \theta, \phi)$.

In addition to this observation, the toroidal resolution requirements increase with N_p , such that edge displacements could not be converged for the $N_p = 5$ case. This is likely due to higher toroidal components of the mode as a result of the mode coupling produced by the $n > 0$ components of the background vacuum magnetic field.

The above observations present a challenge to the use of the VMEC equilibrium approach for physics studies — all of the above equilibria are valid perturbed equilibrium states that could correspond to a saturated ideal MHD mode, so how does one determine the numerical resolution which is most representative of the saturated state produced by the ideal MHD dynamics? This question needs to be addressed before proceeding.

Following the philosophy of Ref. 4, it is proposed to resolve the problem by applying an additional constraint on the solution. Additional constraints have not been added to the convergence algorithm in VMEC; rather, they are used to determine the converged equilibria which are the most physically relevant. In Ref. 33, where fixed current VMEC computations were performed, such that q_{edge} could be modified, an additional physical constraint was used to define the numerical parameters, namely a constant edge safety factor between the unperturbed and perturbed solutions. This constraint is already enforced in iota preserving computations, and so an alternative constraint must be imposed. Two possibilities were explored, using the change in the toroidal plasma current and plasma volume, as shown in Figure 4 (d-f) and (g-i), respectively. It should be emphasised that these constraints are not used to modify the VMEC convergence algorithm. Instead, the adherence of converged computations to these constraints is assessed *a posteriori*, as shown in Figure 4.

The first alternative constraint to identify more realistic solutions could be to ensure that the observed plasma current spike, typically observed during ideal MHD activity, between

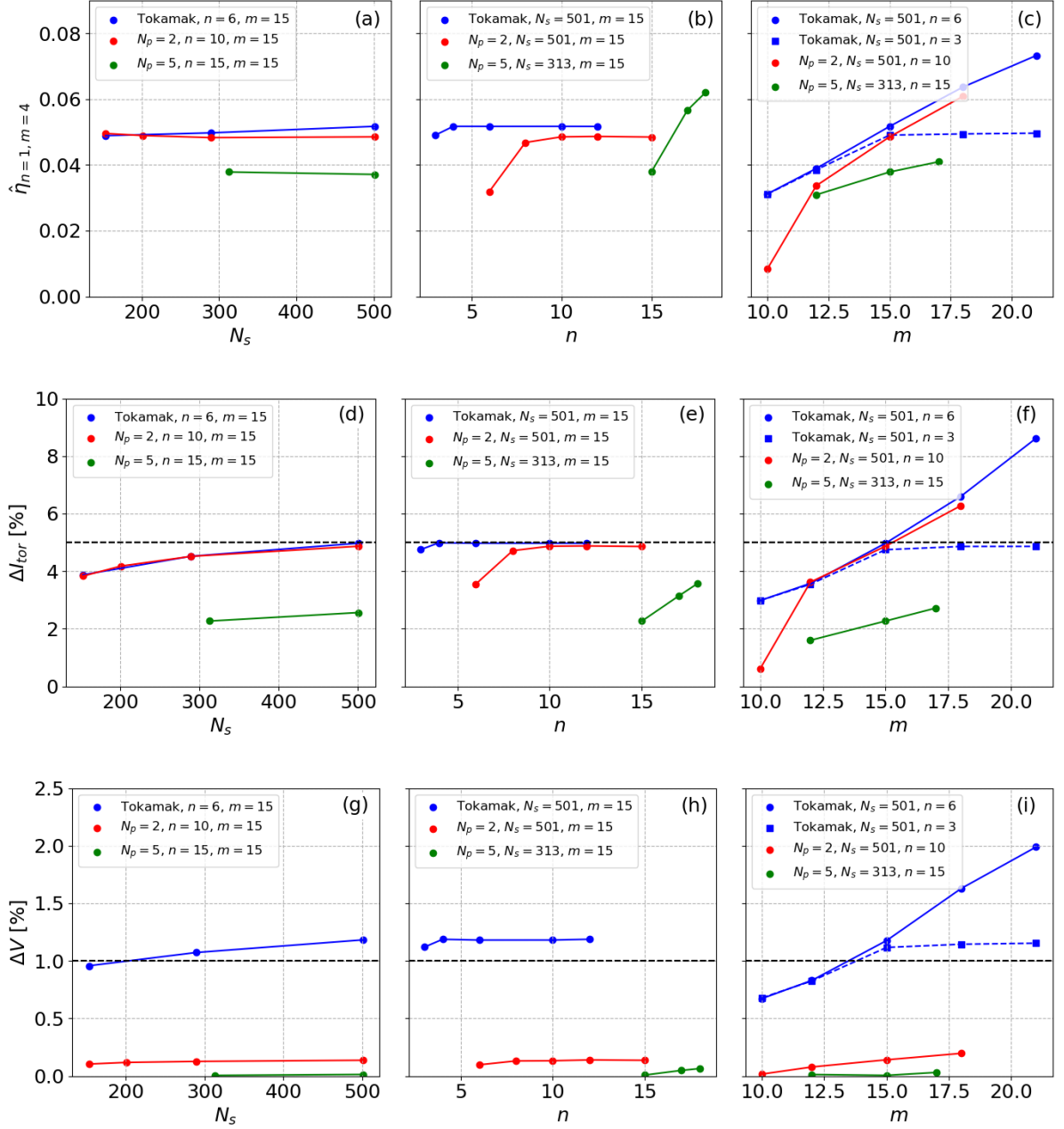


FIG. 4. Resolutions scans for the boundary displacement (a-c), plasma current spike (d-f) and change in plasma volume (g-i) as a function of N_s (a,d,g), m (b,e,h), and n (c,f,i) for tokamak (blue), $N_p = 2$ (red) and $N_p = 5$ (green) stellarator cases with $q_{edge} = 3.9$. The stellarator cases both have $t_{ext} \approx 0.1$.

the perturbed and unperturbed solutions is reasonable in magnitude. For studies which compare to an experiment, the prior knowledge of the experimental current spike can be used to inform the resolution requirements. Unfortunately for this study, there is not a corresponding experiment to compare against, and so it is unclear what the expected current spike should be. For this reason, it is assumed that at $q_{edge} = 3.9$, a current spike on the order of 5 % would be reasonable. The variation of the plasma current spike observed in resolution

scans is shown in Figure 4 (d-f). It can be seen that the current spike remains below 5 % for the tokamak and $N_p = 2$ case when $m \leq 15$, such that results below this value are taken to be more physically meaningful.

A second constraint can be applied by noting the conserved quantities that are found in conventional high aspect ratio orderings of the dynamics in fusion devices. In particular, the incompressibility of the plasma is typically preserved to second order in the aspect ratio²⁴. As a result for the simulated

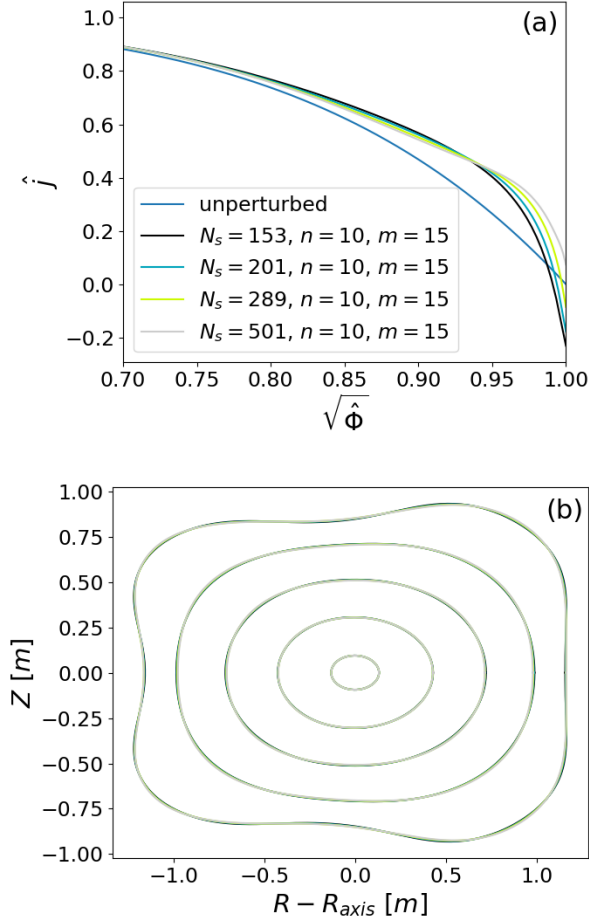


FIG. 5. Variation of the toroidal current density profile, normalised to the value on axis (a) and plasma flux surfaces (b) with increasing N_s for $N_p = 2$ stellarator case with $q_{\text{edge}} = 3.9$ and $t_{\text{ext}} = 0.098$. The radial resolution has a significant effect on the plasma current, and only a weak dependence on the plasma displacement.

cases with $A = 0.1$, it is expected that the plasma volume will be conserved up to $\approx 1\%$. The change in plasma volume is shown in Figure 4 (g-i). For the stellarator cases, the change in plasma volume is relatively small. In the tokamak case, the plasma volume can exceed 1%, with a strong dependence on the poloidal resolution for $m \geq 15$. For this reason, it could be argued that solutions with a lower poloidal resolution are more reasonable.

Formation of current sheets

It is important to also consider the variation and convergence of local quantities, such as the toroidal plasma current density. Convergence difficulties were encountered for free boundary equilibria with $N_s > 501$, and so this is the limit for the radial resolution used for the initial free boundary convergence scan, shown in Figure 4 (a,d,g).

Figure 5 (a) shows the plasma current density and equilib-

rium flux surfaces for the $N_p = 2$ case used in Figure 4 (a). It can be seen that the current does not converge at the plasma boundary, even though the plasma boundary itself is not modified significantly by increasing radial resolution. A similar observation was once again observed in Ref. 33. The response to the plasma deformation in this region is similar to the shielding of magnetic islands that has been observed in previous studies, which has been shown to have significant resolution requirements in VMEC²⁰. However, for the main metrics of interest in this convergence study — the deformation of the plasma — the radial resolution does not appear to be important.

In order to circumvent the high computational cost of free boundary computations, a subset of the converged tokamak solutions from Figure 4 (a) were restarted, keeping the final perturbed boundary fixed, and using a higher radial resolution to assess the influence on the current distribution. A comparison of the original free boundary solution (solid) with the fixed boundary computations (dashed) is shown in Figure 6 (a). The computations with increased radial resolution at $N_s = 2001$ are converged only to $f_{\text{tol}} = 10^{-12}$. The reason that the solutions are very difficult to converge below this value is thought to be because of the formation of current sheets at the plasma boundary, discussed below.

It can be seen that as the poloidal resolution is increased, the enhanced radial resolution indicates that there are localised current sheets at the plasma boundary, as shown in Figure 6 (a). As shown in previous literature considering kink modes in coronal loops^{34,35}, current sheets can be expected to form in proximity to the resonant surface associated with the instability. For an external kink, the current sheet therefore wraps around the outside of the main plasma column, as observed in Ref. 23. The theory in Ref. 24 predicts that negative current sheets should also form at the plasma boundary as a response to the kink deformation on the ideal MHD timescale. In the framework of ideal MHD, these induced current sheets are numerically constrained to the width of the finite grid spacing used to model them, and increase with the resolution applied — they will not dissipate unless a finite resistivity is included in the dynamics²³. In such a way, large localised current sheets are expected according to the physical model implemented in VMEC.

Similar to Ref. 36, the current sheets in VMEC seem to develop as x-points begin to form around the plasma boundary. Figure 6 (b) shows radial contours of the equilibrium in Boozer coordinates for the $m = 10$ case. The Boozer coordinates bend sharply towards the peaks in the perturbed kink. Outside the plasma, in proximity to this region, x-points are expected to form as a result of a (4, 1) magnetic island chain, corresponding to the simulated kink mode in the nonlinear phase.

In order to understand where the current is localised poloidally, the current in the direction of the geometric toroidal angle, \hat{j}_ϕ is computed numerically for this tokamak case. The current is normalised to the value on the magnetic axis. The result is shown for the $m = 10$ case in Figure 7 (a) on the $s = 1.0$ flux surface. The currents are very large, localised in the region where the kink protrudes radially into the plasma

column.

The current sheets that form on the plasma boundary during free boundary VMEC computations can be numerical. For example, in the $m = 15$ case, the current sheet was found to be significantly higher at one poloidal location, as shown in Figure 7 (b). It is likely that such features are unphysical. The calculation of \hat{j}_ϕ requires second order derivatives of the radial splines describing R , Z and λ , making it very sensitive to the sharp changes that occur at the boundary in these equilibria.

The above analysis begins to formulate an alternative argument for constraining the VMEC solution space using the local properties of current sheets at the boundary. The spectral resolution of computations should be limited to prevent the radial Boozer coordinate from bending unphysically towards the x-points outside the plasma boundary, producing unphysical current sheets at the plasma edge. The question remains, how much current is physical, and is the spatial distribution observed in Figure 7 (a) the correct structure for the current sheets to take?

Current sheets are normally limited by resistive diffusion, which is neglected in the ideal MHD formulation of VMEC. The omission of resistivity could be the reason that the saturated kink amplitude is observed to increase indefinitely with increasing spectral resolution. Computations with NSTAB, where the treatment of current sheets is much more accurate, such that lower radial resolutions are tractable, prove to be much more difficult to converge for this reason. In such a way, the authors believe that VMEC is, surprisingly, able to find these nonlinearly perturbed states because of its relatively poor numerical representation of current sheets in the ideal MHD model, limiting their formation to a finite width that allows the solver to converge to $f_{\text{tol}} \leq 10^{-16}$ at lower radial resolution.

The next step is to understand whether the captured current sheet in VMEC is representative of the physical solution, which of course does not conform to the assumptions of ideal MHD. The expected influence of resistivity, or non-ideal diffusive effects, could be a way of ensuring a more physical solution. Doing so requires a detailed understanding of how current sheet formation is influenced by resistivity. To this end, an initial investigation of the current sheets observed in non-linear simulations using the JOEKE code are compared with the results in Figure 7 in Section V D. However this topic merits a separate investigation in its own right, such that further work beyond the preliminary comparisons in this study are necessary to develop the above line of thought into a means of constraining the VMEC computations. This is left for future work. For now, the comparison is used to show that there is qualitative consistency between the current sheets observed in Figure 7 (a) and JOEKE simulations.

Choice of resolution parameters

While the above analysis cannot provide a definitive answer for what the correct resolution parameters are to obtain the most physically meaningful perturbations, the change in

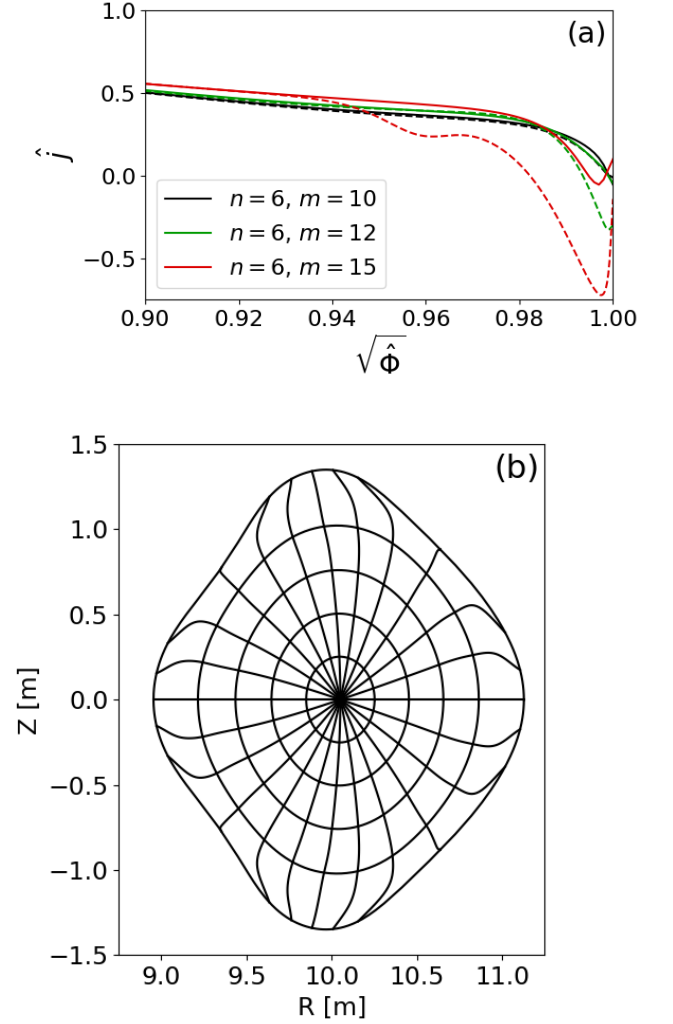


FIG. 6. Variation of the flux surface averaged toroidal current density equilibrium profile at the plasma edge, normalised to the value on axis (a) for perturbed tokamak equilibria with $q_{\text{edge}} = 3.9$, using different poloidal resolutions. The radial resolution is increased from $N_s = 501$ (solid) to $N_s = 2001$ (dashed) with the plasma boundary fixed. The Boozer coordinate representation (b) for the $m = 10$ case shows a strong bending of the radial coordinate towards the poloidal direction, such that constant θ_{Boozer} lines converge towards the peaks in perturbation amplitude, when x-points are expected outside the plasma in the vacuum region.

volume and current spike imply that poloidal resolutions below $m = 15$ are likely to be most reasonable. In the scans of physical parameters which follow, $m = 15$, and $N_s \geq 300$ are used, unless stated otherwise. Although the current sheets for the $m = 15$ case look like they have unphysical numerical structures, this value was chosen because, for the scan of q_{edge} in Section III, it was difficult to obtain saturated states close the upper and lower linear stability thresholds for $m < 15$. This resolution was therefore necessary in order to explore the physical parameter space of the mode in Section III. The toroidal resolution is $n = 6$ and $n = 15$ for the tokamak and

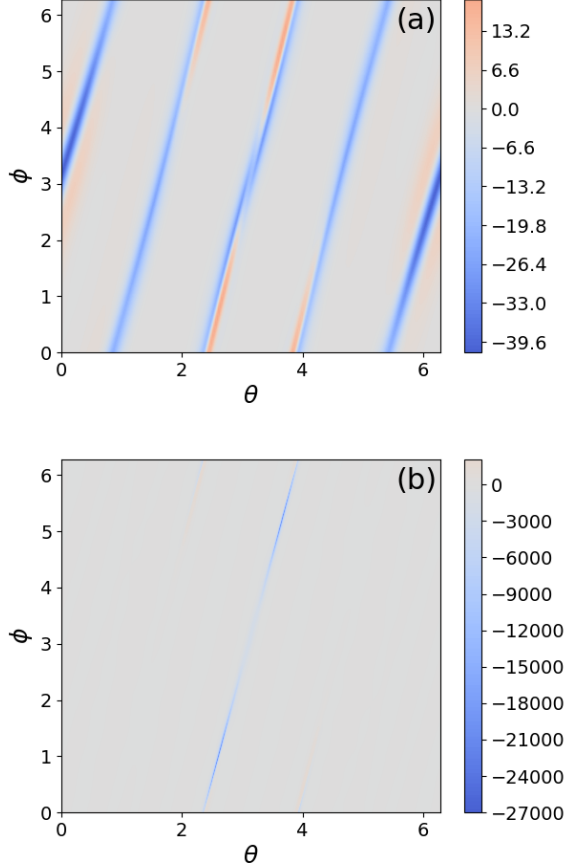


FIG. 7. The computed toroidal current, \hat{j}_ϕ for the tokamak cases studies in Figure 6 on the last closed flux surface. The current is normalised to the value at the magnetic axis in the unperturbed equilibrium. For the $m = 10$, $n = 6$ case (a), the current is strongest in regions where the initial equilibrium is radially perturbed inwards. In this location, the variation in the bending of constant θ_{Boozer} lines is most significant in Figure 6 (b). The toroidal current computed for the $m = 15$ case (b) is much sharper and localised near the high field side midplane, indicating that it is likely numerical, or at least unrealistic.

$N_p = 5$ cases, respectively. Results with different toroidal resolution are computed for the $N_p = 2$ case, to investigate how the spectral resolution can influence the physical trend in the mode structure.

III. DEPENDENCE OF SATURATED MODE AMPLITUDE ON q PROFILE AND ι_{ext}

In this section, VMEC computations are used to carry out parameter scans over the magnetic geometry defined by $q(s)$ and ι_{ext} . The objective of carrying out this analysis is to determine whether the physical trends anticipated from nonlinear analytic theory of kink modes – that the nonlinear mode amplitude is proportional to the linear growth rate – are observed³⁷. Initially, a scan of the q_{edge} was carried out in

the tokamak case. For this scan, q_{edge} is varied by modifying the toroidal flux of the unperturbed equilibrium, keeping the same total toroidal plasma current and current density profile, using $p = 3$. This would be equivalent to adjusting the toroidal magnetic field strength in an experiment.

The q profiles are shown in Figure 8 (a). As expected for a high aspect ratio tokamak case, where B_ϕ is approximately uniform, the increase of the toroidal flux does not significantly distort the shape of the q profile, only shifting it upwards. The flux surfaces of the unperturbed and perturbed surfaces are shown in Figure 8 (b) and (c), respectively. The unperturbed surfaces are shown in order to demonstrate that the shape of the unperturbed, free boundary solution does not significantly change. This is in part due to the use of EXTENDER, as described in Section II, which removes the potential modifications in the plasma shape that could be produced by using a coil set. It can be seen that as q_{edge} approaches 4, the perturbed mode becomes visibly milder in Figure 8 (c).

The amplitude of the dominant (4, 1) perturbation is shown in Figure 9, alongside the normalised linear growth rate of the (4, 1) external kink mode. According to nonlinear analytic theory, the saturated amplitude of the mode should follow the square of the linear growth rate³⁷. This trend is not necessarily expected across the parameter space considered, because the nonlinear analytic result assumes that the mode is marginally unstable. It can be seen in Figure 9 that the general trend of the perturbation amplitude and the linear growth rate are correlated. These results are similar to what has previously been shown in Ref. 12.

It should be noted that, computations were also carried out at $q_{\text{edge}} = 3.55$. At this point in the parameter scan, the ideal MHD mode is stabilised. Only a (3, 1) resistive tearing mode was observed in CASTOR3D. It therefore makes sense that a corresponding saturated (4, 1) mode could not be found at $q_{\text{edge}} = 3.55$. As expected, perturbed states were only found in the window of linear instability of the (4, 1) external kink.

In Figure 9, the nonlinear amplitude of the external kink varies most around $q_{\text{edge}} = 3.9$, such that the mode amplitude appears to be more sensitive in this region of the parameter space. This value of q_{edge} is therefore chosen for scans of $l = 2$ stellarators with increasing external rotational transform, in order to observe the influence of ι_{ext} on the saturated mode amplitude.

In this scan, q_{edge} , and $j(s)$ are once again held constant, while varying the external rotational transform. If the external rotational transform is increased by increasing the $l = 2$ deformation of the equilibrium, keeping other equilibrium parameters fixed, q_{edge} will decrease. In order to keep $q_{\text{edge}} = 3.9$, the toroidal flux is increased to counteract the influence of ι_{ext} increasing. Arguably, a more experimentally relevant parameter scan would have been to keep Φ fixed, as the ι_{ext} is increased via $l = 2$ deformation of the last closed flux surface. This would correspond in an experiment to an increase in the current carried by the $l = 2$ stellarator field coils. However, this would change q_{edge} , which is shown in Figure 9 to have a significant effect on the kink amplitude. To isolate the influence of ι_{ext} from q_{edge} , the toroidal flux is increased instead. Increasing the toroidal flux is no longer a simple increase in

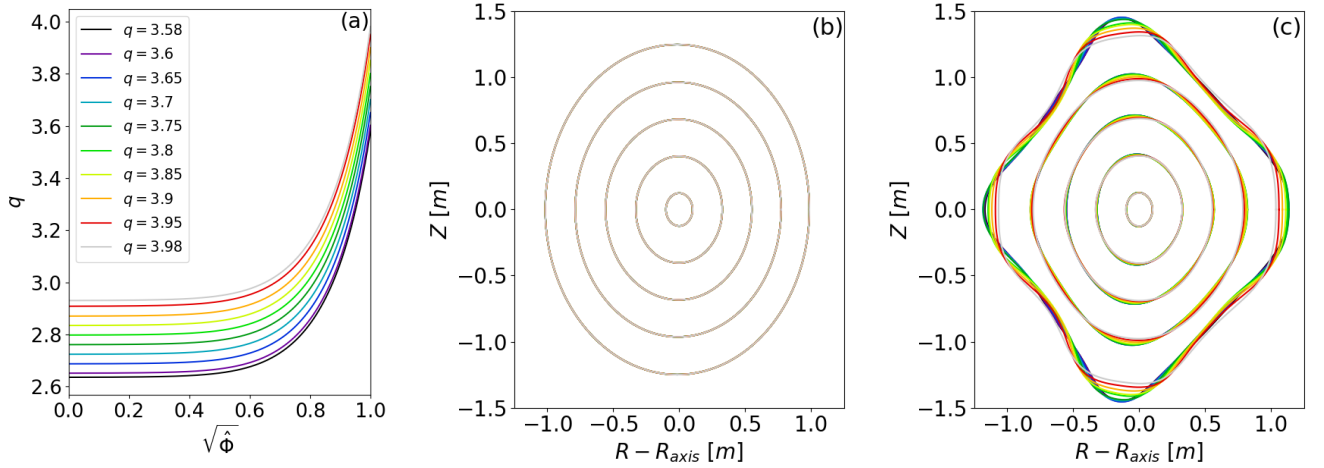


FIG. 8. Plots of the q profile (a), unperturbed (b) and perturbed (c) equilibrium flux surfaces of the saturated states found for the q_{edge} scan in the tokamak limit. The initial flux surfaces are the same for all modelled cases.

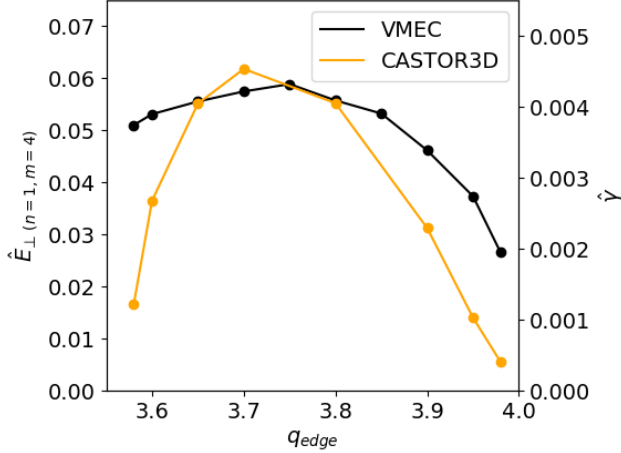


FIG. 9. Scan of edge q for tokamak case. The ι profile was preserved through the computations. The overall amplitude of the $(4, 1)$ component of the perturbation, $\hat{E}_{(n=1, m=4)}$ (black, left axis), follows the same trend as the normalised linear growth rate from CASTOR3D (orange, right axis).

the toroidal magnetic field, as for tokamak cases, because the toroidal flux has an influence on the relative strength of the externally generated poloidal field compared to that generated by the plasma current. However, the scale invariance arguments invoked in Section II are used to make the time scale, mode amplitude, and nonlinear energy spectra of the results comparable. This can be done by normalising these results by the Alfvén time, minor radius, and square of the magnetic field strength, respectively.

The results of scans of t_{ext} for $N_p = 2$ and 5 are shown in Figure 10 and 11, respectively. Once again, the mode amplitudes are compared with the normalised linear growth rates from CASTOR3D. It can be seen that in both cases, a family

of saturated states is found, which is incrementally stabilised by the externally imposed helical field. These states are again observed up to the point at which the $(4, 1)$ mode is observed in the linear stability analysis, which again shows that the linear and nonlinear picture presented by the MHD codes used is, in this sense, consistent.

For the $N_p = 2$ case, a second branch of saturated states were found when using a higher toroidal resolution in VMEC computations. This second series of equilibria have a larger mode amplitude that does not decrease with the linear growth rate. Comparing computations with $n = 10$ and 12, the solutions obtained were similar, as can be expected from the toroidal mode number resolution scan in Figure 4 (b). Because the nonlinear displacement amplitude does not decrease with the linear growth rate, as expected by the nonlinear analytic theory of kink modes³⁷, this is an unexpected result. It is thought that the $n = 10$ states are a second series of bifurcated states which do not correspond to the $(4, 1)$ linear instability. The mode structure of the two branches are compared for the $t_{\text{ext}} = 0.098$ case in the following sections.

IV. NONLINEAR MAGNETIC ENERGY SPECTRA OF VMEC SOLUTIONS

The change in the poloidal magnetic energy spectrum can in principle be used to infer how the magnetic configuration has been modified by the instability, and confirm whether a more energetically favourable state has been reached. It should be noted however that for a free boundary mode, the magnetic energy should in principle be considered over all real space to account for the modification of the energy in the vacuum region. Previous studies have understandably only been able to consider the potential energy over the plasma volume covered by the VMEC computational domain¹⁵. While a method to compute the total energy over all space could not be found, the

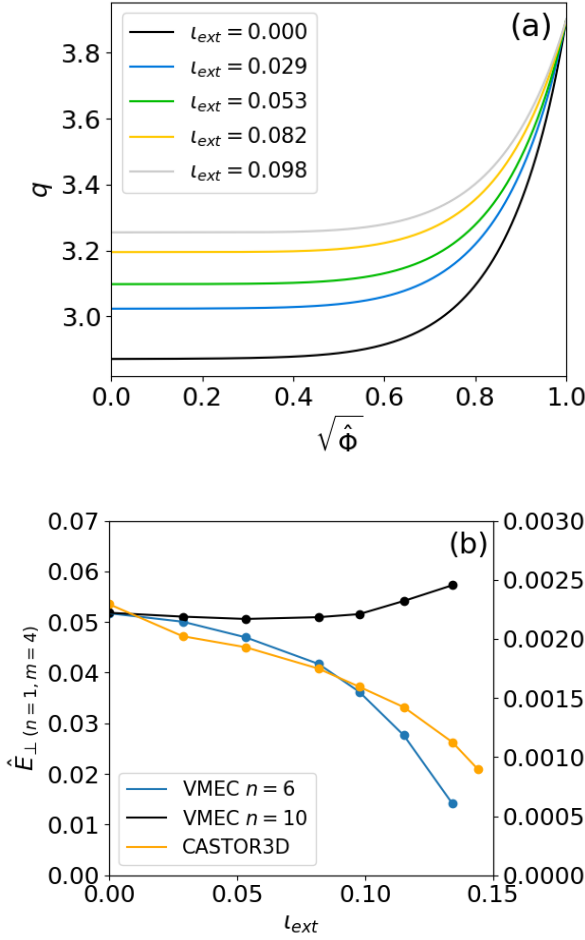


FIG. 10. Modification of the q profile (a) with increasing l_{ext} for $l = 2$ $N_p = 2$ stellarators. The behaviour of the nonlinearly saturated perturbation amplitude (b) with increasing l_{ext} depends on the maximum toroidal mode number used in the computation. The results with $n = 6$ (blue, left y-axis) are considered more physical than with $n = 10$ (black, left y-axis), as the behaviour is correlated with the change in the linear growth rate (orange, right y-axis).

EXTENDER²⁸, NESCOIL²⁹, and MAKEGRID codes could be used to compute the plasma and vacuum magnetic fields in a finite domain both inside and outside the plasma volume on a R, Z, ϕ grid. This enables an assessment of the modification of the magnetic field structure in the vacuum region close to the plasma, where the interaction should be strongest. Note that previous code comparisons, such as in Section 2.2.5 of Ref. 19, show numerical errors in the computation of the magnetic field can lead to numerical island structures. For the comparison of the global mode structure, these local errors around rational surfaces are not considered to be significant.

The magnetic field is computed and Fourier decomposed inside a cylindrical torus, centred at $R = 10$, with minor radius, $r_{\text{minor}} = 1.75$. This torus contains all of the simulated cases considered in the parameter scans from Section III. An example of the Fourier decomposed radial magnetic field, B_R , for an unperturbed $l = 2$, $N_p = 2$ stellarator is shown in Figure

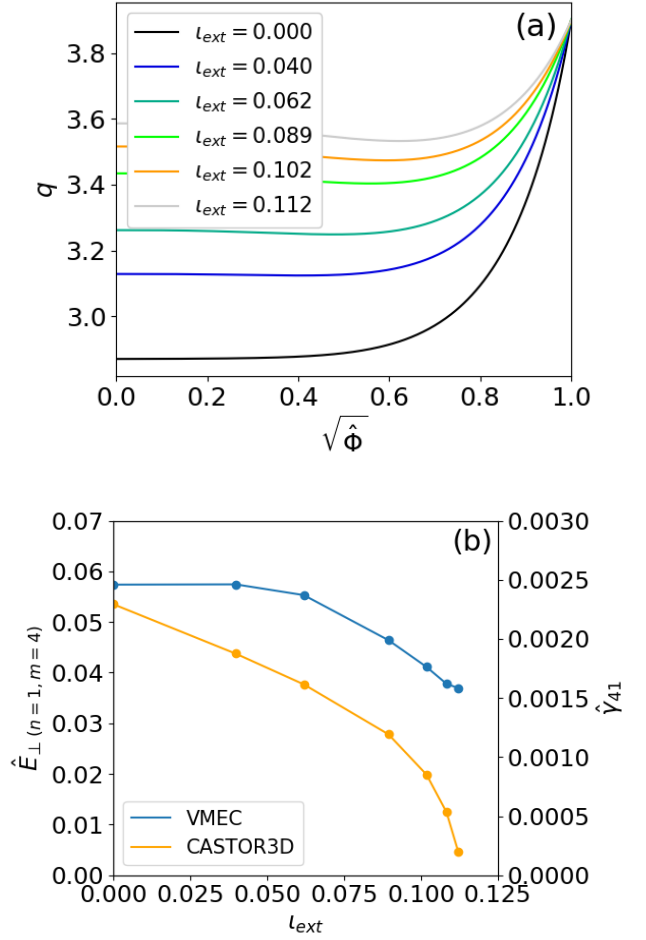


FIG. 11. Modification of the q profile (a) with increasing l_{ext} for $l = 2$ $N_p = 5$ stellarators. In (b) it is shown that the nonlinearly saturated perturbation amplitude (blue, left y-axis) decreases with the linear growth rate (orange, right y-axis). Note that computations at higher spectral resolution were not possible for this case, due to the demanding computational requirements.

12. It should be noted that the $n = 2$ component of the equilibrium magnetic field is larger than the $n = 0$ component, indicating that it contributes a significant part of the equilibrium poloidal magnetic field.

The poloidal magnetic energy spectrum is then computed, normalising by the square of the volume averaged toroidal magnetic field such that results of different equilibrium computations can be compared with one another. The results for three cases with different field periodicities are shown in Figure 13. The external rotational transform is ≈ 0.1 for the stellarator cases in Figure 13 (b) and (c). It can be observed that the energy in the perturbation is notably smaller in the stellarator cases.

In the tokamak case, the magnetic energy cascades from high values in low toroidal harmonics to lower values as n increases. For stellarators however, it can be seen that the perturbation exists predominantly in the $N_f = 1$ mode family of the simulated device. This means that the energy corresponding

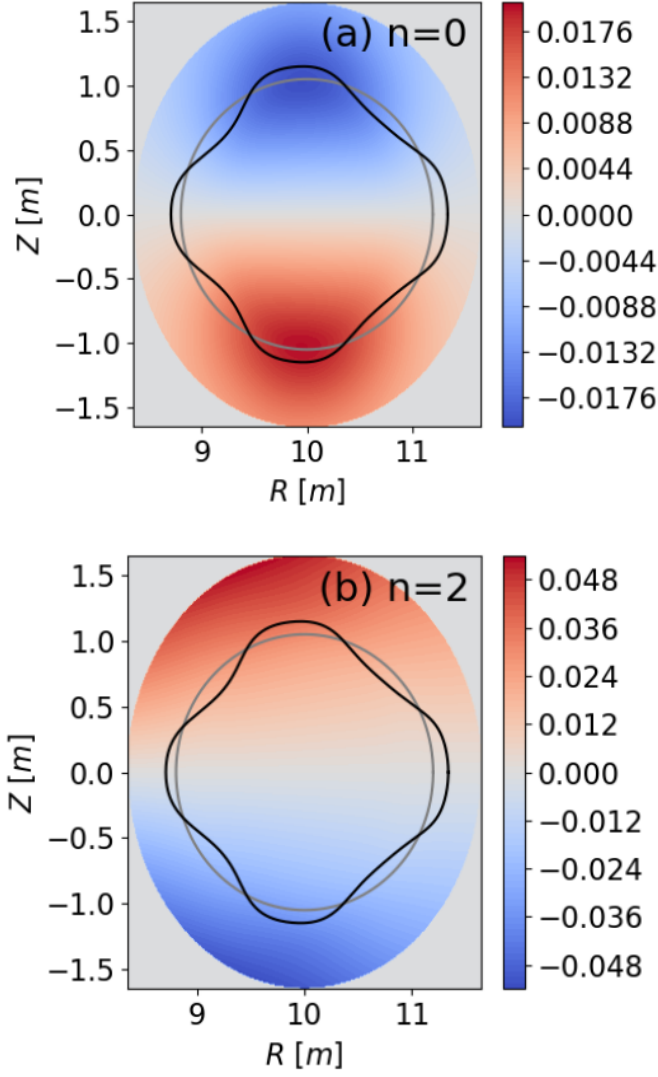


FIG. 12. $n = 0$ (a) and $n = 2$ (b) Fourier components of the total radial magnetic field, \hat{B}_R , normalised by the volume averaged magnetic field of the initial equilibrium. The field is computed within a cylindrical torus enclosing the plasma volume in the $\phi = 0$ plane for a $l = 2$, $N_p = 2$ stellarator with $t_{\text{ext}} = 0.029$. The initial (grey) and perturbed (black) plasma boundary are overlaid on the data.

to the perturbation cascades down from the dominant $n = 1$ mode to $n = 3, 5$, and so on in the $N_p = 2$ case. Equally in the $N_p = 5$ case, the $n = 4$ and $n = 6$ modes are notably larger than the members of the $N_f = 2$ mode family. These results are expected due to the toroidal mode coupling of the instability in stellarators.

The $n = 0$ poloidal magnetic energy has increased in all cases. This is unintuitive, because the overall energy of the plasma-vacuum system should decrease as a result of the MHD perturbation. The $n = 0$ energy provides the drive for the MHD instability, such that the overall energy in this mode is expected to decrease as a result of the nonlinear perturbation, despite the increase in plasma current, observed in Fig-

ure 4 (d-f). A further unexpected observation is that W_{mhd} of the nonlinearly saturated state is observed to increase when compared to the initial unperturbed state in VMEC computations that conserve helicity. At first glance this result might be considered concerning, but can be justified by studying the exchange of energy between the plasma and vacuum as considered in Section V C.

In contrast, the $n > 0$ toroidal harmonics of the $N_f = 0$ mode family show a decrease in poloidal magnetic energy for the $N_p = 2$ and the $N_p = 5$ stellarator results. It could be argued that these toroidal harmonics contribute to the equilibrium drive for the instability, which releases energy from these toroidal harmonics in the perturbed state.

V. COMPARISON WITH NONLINEAR JOREK SIMULATIONS

Two questions are introduced by the above observations - why does the $n = 0$ energy increase in all cases, while the $n > 0$ components of the $N_f = 0$ mode family decrease for stellarator cases? With respect to the $N_p = 2$ case, which physical trend observed for the dependence of the saturated mode amplitude on t_{ext} in Figure 10 is correct?

In order to develop answers to these questions, the VMEC results are compared with nonlinear simulations using the JOREK code. The recent extension of JOREK²¹ to consider stellarators is briefly introduced in Section V A. In Section V B, the simulation set up for both tokamak and stellarator simulations is described. The increase in the $n = 0$ magnetic energy is studied in Section V C. In Section V D, the current sheet formation during the external kink is shown, comparing with the VMEC results in Figure 7. Finally, the influence of the non-axisymmetric vacuum field on the mode amplitude is considered in Section V E, to demonstrate that the mode amplitude is expected to decrease with increased t_{ext} .

A. Extension of the JOREK code to study stellarators

In this section, the reduced nonlinear MHD model for stellarators, implemented in JOREK, will be briefly described, highlighting some of the similarities and differences with the reduced MHD model used for tokamaks, described in Ref. 14. For stellarators, the reduced MHD ansatz for the magnetic and velocity field are given by

$$\mathbf{B} = \nabla\chi + \nabla\psi \times \nabla\chi \quad (4)$$

$$\mathbf{v} = \frac{\nabla\Phi \times \nabla\chi}{B_v^2}. \quad (5)$$

This ansatz is similar to the reduced tokamak model implemented in JOREK, neglecting parallel flow, which is a second order quantity in the reduced ordering of high aspect ratio current driven external kink modes²⁴. The main difference is that

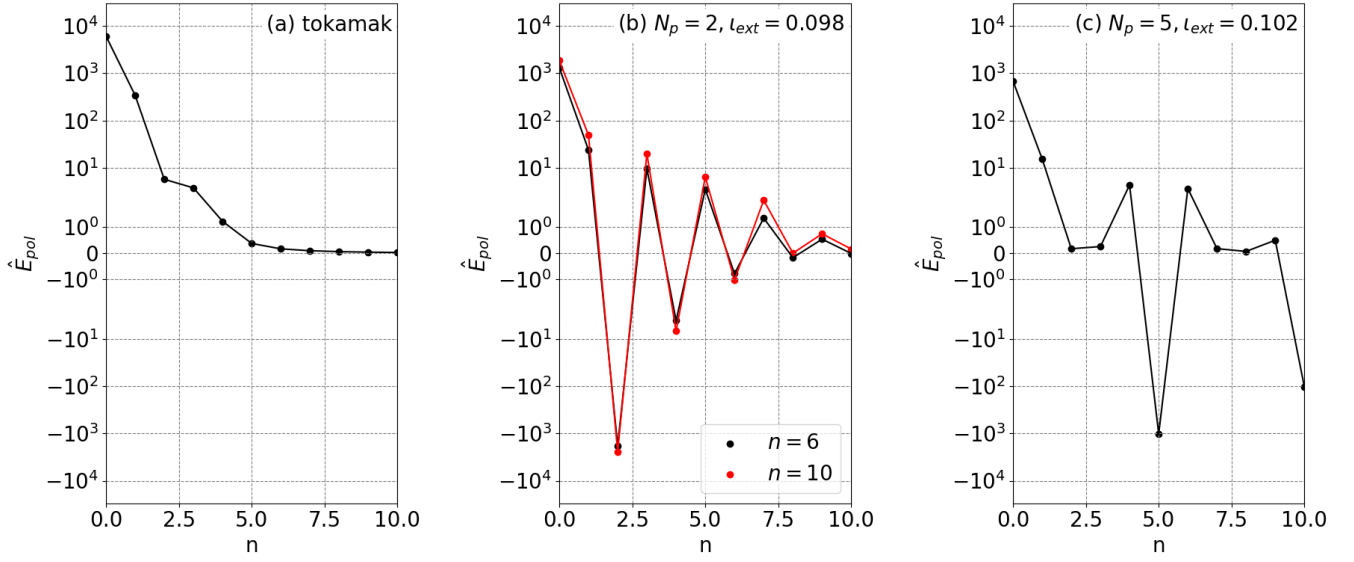


FIG. 13. Normalised perturbed poloidal magnetic energy, \hat{E}_{pol} , of the tokamak (a), and $l = 2$ classical stellarators with $N_p = 2$ (b) and $N_p = 5$ (c) at $q_{edge} = 3.9$. The energies are integrated over a circular torus, centred at $R = 10.0$, with radius, $r_{minor} = 1.75$, which fully encloses the plasma volume of all cases. \hat{E}_{pol} is normalised by the volume average magnetic field strength squared from the unperturbed equilibrium, such that the three cases can be compared quantitatively.

the toroidal magnetic field $F_0 \nabla \phi$ is replaced by the vacuum scalar potential, χ , representing the vacuum magnetic field, generated by external currents. The single temperature time evolution equations for the evolved variables for the poloidal flux, potential, density and temperature ($[\psi, \Phi, \rho, T]$) are

$$\frac{\partial \rho}{\partial t} = -B_v \left[\frac{\rho}{B_v^2}, \Phi \right] + \nabla \cdot (D_\perp \nabla_\perp \rho + D_\parallel \nabla_\parallel \rho) + S_\rho \quad (6)$$

$$\begin{aligned} \nabla \cdot \left(\frac{\rho}{B_v^2} \nabla^\perp \frac{\partial \Phi}{\partial t} \right) &= \frac{B_v}{2} \left[\frac{\rho}{B_v^2}, \frac{(\Phi, \Phi)}{B_v^2} \right] + B_v \left[\frac{\rho \omega}{B_v^4}, \Phi \right] \\ &\quad - \nabla \cdot \left(\frac{P}{B_v^2} \nabla^\perp \Phi \right) + \nabla \cdot (j \mathbf{B}) \\ &\quad + B_v \left[\frac{1}{B_v^2}, p \right] + \nabla \cdot (\mu_\perp \nabla^\perp \omega) \\ &\quad - \Delta^\perp (\mu_{num} \Delta^\perp \omega) \end{aligned} \quad (7)$$

$$\begin{aligned} \rho \frac{\partial T}{\partial t} &= -\frac{1}{B_v} [\rho T, \Phi] - \gamma \rho T B_v \left[\frac{1}{B_v^2}, \Phi \right] \\ &\quad + \nabla \cdot \left[\kappa_\perp \nabla_\perp T + \kappa_\parallel \nabla_\parallel \nabla_\parallel T \right. \\ &\quad \left. + \frac{p D_\perp}{\rho} \nabla_\perp \rho + \frac{p D_\parallel}{\rho} \nabla_\parallel \rho \right] \\ &\quad + (S_e + \eta_{ohm} B_v^2 j^2) - T \frac{\partial \rho}{\partial t} \end{aligned} \quad (8)$$

$$\frac{\partial \psi}{\partial t} = \frac{\partial^\parallel \Phi - [\psi, \Phi]}{B_v} - \eta (j - j_{source}) + \nabla \cdot (\eta_{num} \nabla^\perp j), \quad (9)$$

where the auxiliary variables for the plasma current, j , and the plasma vorticity, ω , are given by

$$j = \Delta^* \psi \quad (10)$$

$$\omega = \Delta^\perp \Phi. \quad (11)$$

The operators used in the above equations are the same as those defined in Ref. 22. The equations are again similar to the simplest reduced tokamak model in JOREK. The model outlined above and in more detail in Ref. 22 is currently being extended to include further physics, such as separate ion and electron temperatures. In the remainder of this section, the simulations using both the tokamak and stellarator model in JOREK in Section V C and V E will be described in more detail.

B. JOREK simulation set up and parameters

For the simulation of external kinks in a tokamak used in Section V C to understand the increase in $n = 0$ poloidal magnetic energy. A free boundary equilibrium is required to capture the exchange of energy between the simulation domain and vacuum region. This is achieved using the JOREK-STARWALL coupling³⁸, which has been applied, and benchmarked successfully for the study of vertical displacement

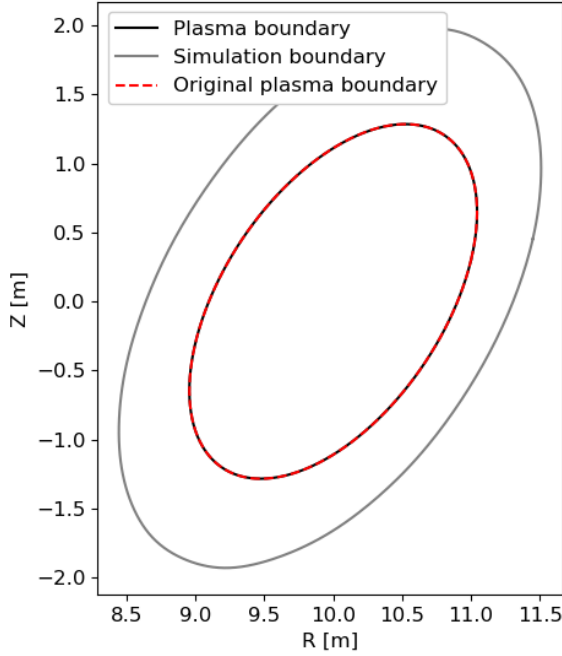


FIG. 14. Simulation and plasma boundary of free boundary VMEC equilibrium computations. The initial VMEC computation, ending the computational domain at the plasma boundary, compares well with the plasma boundary obtained at an internal flux surface, when the equilibrium computational boundary is extended into an artificial vacuum region around the plasma, with zero current and a small, finite pressure.

events, and is currently undergoing validation against experimental results.

The STARWALL coupling has not yet been included in the stellarator model, and so in Section V E, this limitation is circumvented by extending free boundary VMEC equilibria into the vacuum region, shifting the computational boundary, such that it is sufficiently far from the plasma boundary to observe the mode. An example of the modified simulation boundary, along with the position of the plasma boundary is shown in Figure 14. The original plasma boundary from the computation without the extension of the computational domain is also shown to demonstrate the modification of the internal flux surfaces is negligible.

To determine how much the computational domain needed to be extended beyond the plasma boundary to still observe the external kink mode, CASTOR3D computations were carried out in the presence of an ideal wall, as shown in Figure 15. In these computations, the wall distance was varied as a function of the original plasma boundary Fourier coefficients, by scaling the coefficients by the factor r_{wall} . It was found that the $N_p = 5$ device is more strongly influenced by the wall, such that the domain boundary needed to be scaled by a factor $r_{\text{wall}} = 1.6$ in this case. For the $N_p = 2$ case, $r_{\text{wall}} = 1.5$ was chosen in order to approach the no wall limit. Larger extensions were difficult to compute without causing the plasma

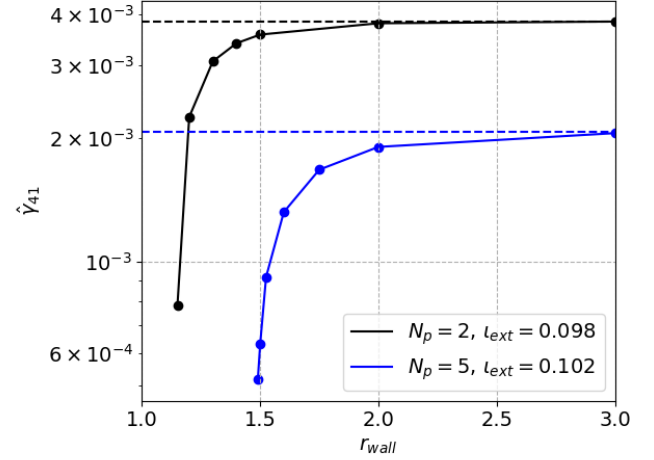


FIG. 15. Linear growth rates of the (4, 1) external kink mode for two and five field period stellarators, as a function of the ideal wall distance. r_{wall} is a scaling factor used to construct the ideal wall from the plasma boundary Fourier representation. It should be noted that the growth rate in the ideal wall limit is different from Figure 10 and 11, because these results assume a constant density.

boundary to shift from its original position.

The viscoresistive and diffusive parameters used in simulations are shown in Table I. The spatial dependencies of these parameters, in particular resistivity and viscosity, are known to influence the trajectory of the nonlinear solution²³. Unlike in Ref. 14, the Spitzer-like resistivity is not modified to include a highly resistive vacuum region. Because the difference in boundary conditions already leads to a quantitative difference in the dynamics, the purpose of this study is to provide a qualitative comparison to understand the mechanism behind the mode structures observed. A constant parallel heat transport coefficient is also used to ease the toroidal resolution requirements - in stellarator simulations, it is observed that a large number of toroidal modes are necessary to accurately capture thermal transport. This is because of the high resolution required to capture the VMEC magnetic field representation, as shown in Ref. 39. A parallel diffusivity is also applied to replace the parallel particle transport from advection, which has been neglected. For the $N_p = 5$ case, it is found that with 20 toroidal harmonics, the equilibria are converged with no artificial transport generated by the truncation of the Fourier representation of the magnetic field from GVEC⁴⁰.

Obtaining stationary profiles is a further complication of stellarator simulations. Typically in tokamak simulations, an axisymmetric initial phase is carried out, in order to obtain stationary profiles, before proceeding to model the instability. Admittedly, for the simulated tokamak case, the steady state profiles could not be computed, because the elliptically shaped tokamak equilibrium is vertically unstable. The vertical displacement event would evolve on a much faster time scale than it would take for the equilibrium to reach steady state. For this case, it is necessary to initialise the $n > 0$ modes before the profiles have fully equilibrated. For the aspects of

TABLE I. Parameters used in nonlinear JOREK simulations of tokamak and stellarators. Unless stated, values are in JOREK normalised units.

Parameter	Tokamak	$l = 2$ Stellarator
T [eV]	0.216 – 648.4	0.216 – 648.4
n [$\times 10^{20}$]	0.03 – 1.0	0.03 – 1.0
κ_{\parallel}	1.0	1.0
κ_{\perp}	10^{-6}	10^{-6}
D_{\perp}	10^{-6}	10^{-6}
η [$\Omega \cdot m$]	1.9382×10^{-7}	1.9382×10^{-7}
η_{num} [$\Omega \cdot m^3$]	1.9382×10^{-12}	1.9382×10^{-14}
μ [$kg \cdot m^{-1} \cdot s^{-1}$]	5.1594×10^{-8}	5.1594×10^{-8}
μ_{num} [$kgm \cdot s^{-1}$]	5.1594×10^{-13}	5.1594×10^{-15}
n_{rad}	143	64
n_{pol}	86	48
n_{plane}	32	64 – 128

the dynamics that we are interested in, namely the flows of magnetic energy on the fast ideal MHD timescale, the much slower relaxation of the profiles is not considered to have an effect.

For stellarator simulations, the $N_f = 0$ mode family can also not be eliminated from simulations. Although the simulations are fixed boundary, such that vertical displacement events are not a concern, higher mode number instabilities from the $N_f = 0$ mode family can be triggered before the profiles become stationary. Fortunately, in this study, $N_f = 0$ mode activity was not observed, such that the initial equilibrium could be relaxed to an approximate steady state. The $N_f = 0$ mode families were run for approximately 10 ms, before initialising a full torus simulation.

C. Understanding the increase in $n = 0$ poloidal magnetic energy

To understand the increase in the $n = 0$ energy in the VMEC results, a free boundary JOREK equilibrium was constructed of the tokamak case with $q_{\text{edge}} = 3.9$. This equilibrium was then evolved with free boundary conditions applied to all toroidal harmonics. As previously stated, the difficulty in doing this is that the equilibrium is vertically unstable, and vertical position control could not be applied as this would affect the energy analysis. However, the external kink was found to grow sufficiently fast for this case, that a vertical displacement event was not observed over the simulated timescale, such that the observed $n = 0$ dynamics are purely a result of the external kink saturation.

To further develop an understanding of the $n = 0$ poloidal magnetic energy increase observed in the corresponding VMEC result, the evolution of the poloidal magnetic energies is shown in Figure 16. It can be seen in Figure 16 (b) that as the $n = 1$ external kink saturates, an increase in the $n = 0$ energy is observed, similar to in VMEC computations. To confirm that this observation is related to the finite integral over the simulation domain, which does not capture all of the energy in the free boundary system, a simulation is also

run applying a fixed boundary condition to the $n = 0$ poloidal flux. With this boundary condition, the $n = 0$ energy does not increase. The result is expected because the fixed boundary implies that the simulated domain is a closed system, such that the total magnetic energy cannot increase as a result of the instability. Finally, the Poynting flux on the JOREK boundary is computed in the free boundary simulation case, as shown in Figure 16 (c). This diagnostic shows that there is a flux of magnetic energy into the system from outside of the JOREK computational domain.

The fixed boundary simulation, and the Poynting flux diagnostic confirm that the increase in the $n = 0$ energy in JOREK is due to an exchange of energy between the integrated volume, and the vacuum region. While equivalent diagnostics could not be identified to confirm this for the VMEC result, it is likely that the increase in the $n = 0$ magnetic energy in Figure 13 is a result of the same effect. A similar test could not be carried out for the stellarator cases, as free boundary conditions have currently not been implemented for the stellarator models in JOREK, however the dynamics are expected to be similar for the computed classical stellarator equilibria.

The exchange of energy is likely due to the changing current profile, and total plasma current. To first order, the confined plasma can be treated as a current carrying loop. If such a current loop has an increasing current, similar to the spike in current observed in the VMEC result, the induced Poynting flux will be towards the current loop. While the rearrangement of current in VMEC and JOREK results is more complex than such a simplified case, the first order effect of the dynamics should be similar, explaining the increase in the $n = 0$ energy in the integrated region. This analogy breaks down when considering the energy over all space, which would increase in the case of a loop with increasing current. In the case of the external kink, it is expected that the total energy would decrease because of changes in the spatial current distribution, leading to an effective change of the loop inductance.

D. Comparison of current sheet locations and amplitudes in JOREK and VMEC

For comparison with the current sheets observed in Figure 7 in VMEC, the toroidal current in JOREK units is plotted in Figure 17 at two time points during the initial saturation dynamics. Counterflowing currents, in the opposite direction to the current on axis, are located in proximity to the plasma edge at both time points. Broad counterflowing current sheets are observed near the x-points of the (4, 1) magnetic islands, where the kink protrudes most radially outwards, as well as much finer current sheets at the region where the kink is radially perturbed inwards. The reason that the current sheets at the x-points are broader is because they are outside the plasma where the resistivity is relatively large, such that the current sheets induced in this region are diffuse. Because these current sheets are outside of the plasma region, it is expected that these current sheets would not be observed in VMEC.

The current sheets in the region where the kink is radially perturbed inwards resemble the sheets observed for the

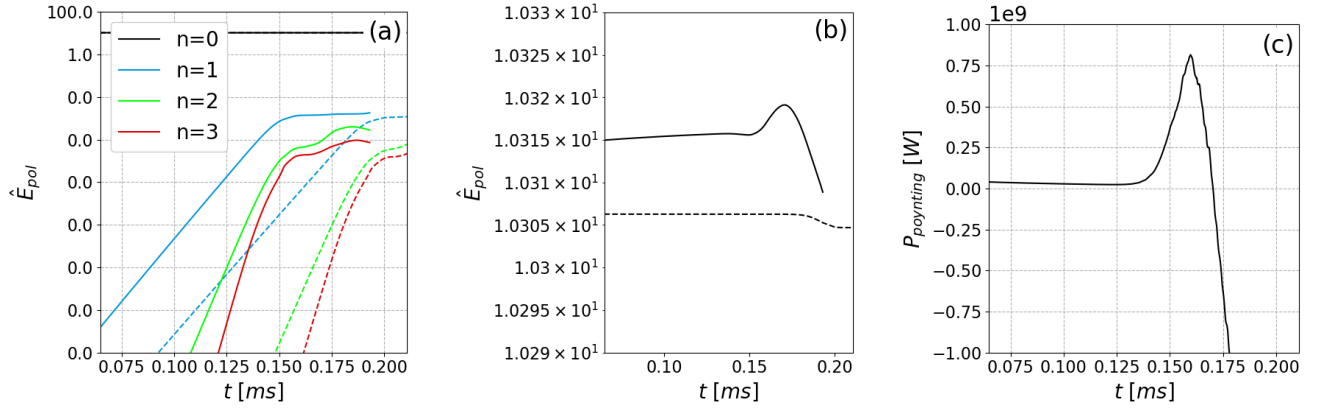


FIG. 16. Evolution of poloidal magnetic energy spectrum (a and b) in $n = 0$ free (solid) and $n = 0$ fixed (dashed) boundary JOREK simulations of the tokamak test case modeled in VMEC with $q_{edge} = 3.9$. The Poynting flux (c) into the free boundary JOREK simulation domain indicates the increase in $n = 0$ integrated poloidal magnetic energy comes from the vacuum region. The grey dashed line shows the point in time that Figure 17 corresponds to in the free boundary simulation.

VMEC computation in Figure 7 (a). These sheets are thinner, because the temperature remains high, so that they have a smaller width and are much more difficult to resolve. To confirm that the sheets are localised on the initial plasma boundary, a Poincaré is overlaid on the current pseudocolour plot in Figure 18. Each field line is coloured based on the value of q computed numerically by tracing the field for 200 toroidal turns. In such a way, points with $q < 3.9$ can be used to identify the approximate region corresponding to the plasma boundary. It can be seen from the Poincaré in Figure 18 that the current sheet lies within the plasma volume, intersecting with field lines in the range of $q = 3.65 - 3.8$. It has proved very difficult to identify field lines with $q = 3.9$, because the value of q sharply transitions from 3.5 to 4 in the edge region. The above observations indicate that the current sheets in the VMEC result in Figure 7 (a) are consistent with JOREK in the early nonlinear phase.

Later during the nonlinear saturation, shown in Figure 17 (b), positive and negative sheet currents are also present, which are poloidally localised in the regions where the kink is radially protruding outwards. Such structures are not observed in VMEC. It should be noted however that these sheets occur a finite time after the initial saturation, and are thought to be due to the competition of the $(4, 1)$ mode with instabilities dominated by $n > 1$. For example, a $(7, 2)$ and $(8, 2)$ structure can be observed in Poincaré plots computed at $t = 0.160$ ms, shown in Figure 19. As argued in previous work¹⁴, similar island structures triggered by nonlinear mode competition are suppressed by the assumption of nested flux surfaces in VMEC.

It is believed that it is the nonlinear interaction of these modes which results in these secondary current sheets, occurring later in time, and as such they should not be expected in the VMEC result. It could be argued that the difficulty in converging current sheets towards relatively smooth structures like those in Figure 7 (a) is a result of the shielding currents that might be necessary to prevent the $(7, 2)$ and $(8, 2)$ island

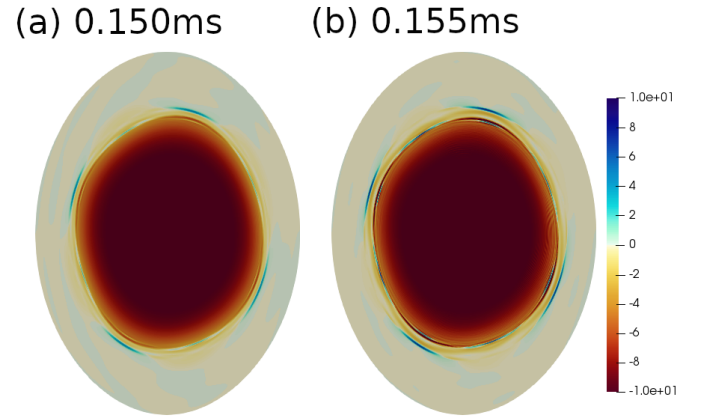


FIG. 17. The current density $j = Rj_\phi$ in the $\phi = 0$ poloidal plane at $t = 0.150$ ms (a) and $t = 0.155$ ms (b) of the free boundary tokamak simulation in JOREK. Negative current sheets are observed on and near the plasma boundary.

structures from forming close to the plasma boundary. A more detailed investigation would be necessary to confirm this.

The above analysis indicates that the current sheets observed in VMEC and JOREK during the early nonlinear phase are qualitatively consistent. This is encouraging for the use of both approaches. It should be acknowledged that neither solution is perfect. The viscoresistive parameters in the JOREK simulations can be higher than experimentally relevant values due to computational limitations. The ideal MHD assumption enforced in VMEC must eventually break down near the edge of the plasma, as the temperature falls, such that the current sheets are not appropriately constrained without limiting the resolution parameters.

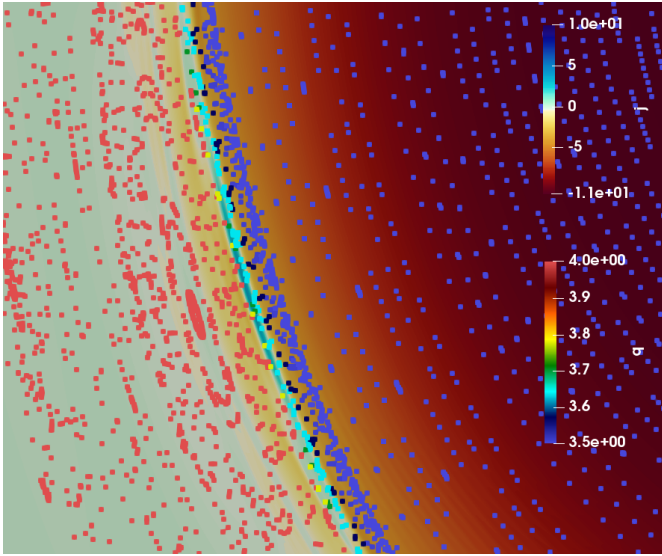


FIG. 18. Zoom in of the plasma boundary region of Figure 17 (left) at $t = 0.150$ ms. A Poincaré plot is overlaid, labelling each line by its approximate q value. In such a way, it can be seen that the current sheets are found in a region where $q < q_{\text{edge}} = 3.9$ such that they can be expected on the plasma boundary.

E. Comparison of the influence of t_{ext} on the perturbation amplitude

As discussed in Section III, the dependence of the perturbation amplitude on t_{ext} in VMEC can have different behaviours depending on the spectral resolution used. In this section the trend in the perturbation amplitude of JOREK simulations is qualitatively compared with that in VMEC. The evolution of the poloidal magnetic energies, split into mode families is shown in Figure 20 for $l = 2$, $N_p = 2$ stellarators with $t_{\text{ext}} = 0.053$ (a) and $t_{\text{ext}} = 0.098$ (b). The energies are normalised by the volume averaged magnetic field to account for variations in the initial equilibrium energy.

It can be seen in Figure 20 that the linear evolution of the mode has the expected exponential growth in both cases, indicating that the equilibrium profiles are not being modified on the time scale of the instability. With respect to the initial saturation of the mode, grey horizontal dashed lines are used to indicate the initial saturation amplitude of the $n=1$ mode. It can be seen that the case at $t_{\text{ext}} = 0.098$ saturates at a lower amplitude. The difference is however marginal, and could be influenced by the nonlinear dynamics that are triggered in these cases.

As indicated by the relative amplitude of the kinetic energies attributed to the two mode families, the $N_f = 0$ mode family seems to have been triggered by the presence of the $n = 1$ dominant kink mode. Evidence of this can be seen by visualising the perturbed plasma temperature during the nonlinear phase for the $t_{\text{ext}} = 0.098$ case, as shown in Figure 21. The two plots correspond to time points during the initial saturation, and approximately 1 ms after. It can be seen that after the initial saturation of the $(4, 1)$ kink mode, a $(7, 2)$ magnetic

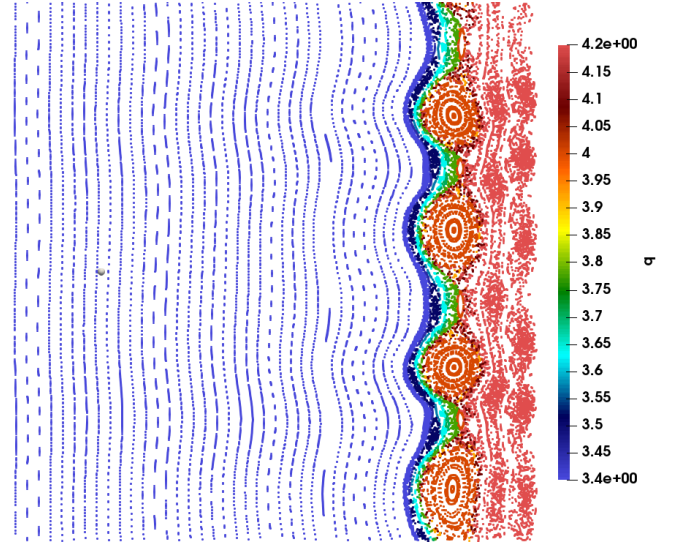


FIG. 19. Poincaré plot at $t = 0.161$ ms for the free boundary tokamak case in Figure 16 (a). Field lines are labelled by their approximate q value. A secondary $(7, 2)$ island structure (dark blue) has formed, and there is a competing $(8, 2)$ island structure outside the plasma. These competing modes are thought to be the reason for additional current sheets in the JOREK solution in Figure 17 (right) at $t = 0.155$ ms. A different time point was chosen for this Poincaré plot, because the island structures were easier to identify.

island structure appears near the plasma edge.

It should be noted that the simulation results above are preliminary, and require further work to resolve some outstanding issues in the simulation set up. Further investigations are certainly necessary to improve the quality at which the ideal dynamics of the external kink modes are represented. This task, and a more detailed investigation of the nonlinear dynamics are the subject of future work.

VI. CONCLUSION

Free boundary equilibrium computations of external kinks in tokamaks and classical stellarators have been used to gain an understanding of the expected mode structure in simple external nonlinear MHD perturbations. A parameter space of Ohmic, Wesson-like current profiles, with different ellipticities has been identified where saturated states can be robustly computed. In the author's experience, a small amount of ellipticity is required to achieve a saturated state, which converges well to low force tolerances.

Numerical resolutions scans could not be converged to a single nonlinearly saturated state with increasing spectral resolution. Current sheets are observed at the plasma boundary of VMEC computations, which grow to arbitrary size depending on the grid resolution parameters. This is expected from the logic of Ref. 23, where it was shown that the saturation mechanism of an external kink requires some resistive diffusion to eventually dominate as strong current sheets form on the plasma boundary. The authors would argue that the rea-

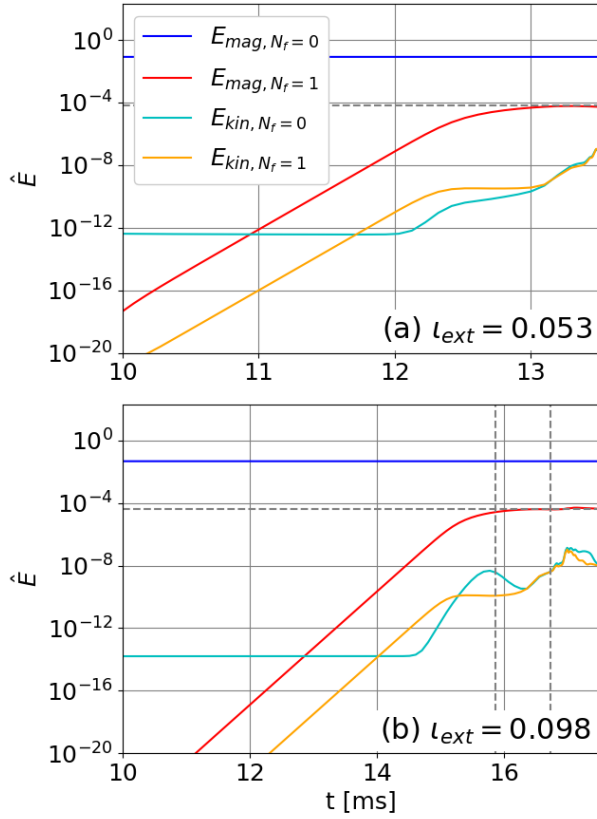


FIG. 20. Evolution of the poloidal magnetic energies of $l = 2$, $N_p = 2$ stellarators with $t_{\text{ext}} = 0.098$ and $t_{\text{ext}} = 0.053$. The energies are split into the two different mode families to compare the overall energy associated with the initial $n = 1$ saturation. The horizontal grey dashed line marks the approximate initial saturation amplitude. The vertical grey dashed lines correspond to the time points of the Pseudocolour plots in Figure 21.

son VMEC is able to capture these nonlinearly saturated states so well is because the numerical scheme requires significant resolution to capture the induced currents, essentially replacing the physical diffusive process through resistivity with artificial diffusion. As such, the toroidal and poloidal Fourier spectra need to be chosen carefully in order to obtain a physically meaningful result. In this work, additional physical constraints, using the observed plasma current spike and conservation of volume are used to identify which modes should be included in the Fourier spectra.

Considering the nonlinear mode structure of the energy spectrum in more detail, tokamak and stellarator results differ in that the perturbed energy is carried predominantly in the $N_f = 1$ mode family of stellarator cases. This qualitative difference can be expected given the toroidal mode coupling introduced by the increased field periodicity. The normalised poloidal magnetic energy perturbation of the considered stellarator cases are lower than the equivalent tokamak case with the same q_{edge} . This indicates that the initial ideal saturation dynamics are milder than in the tokamak case.

It has been shown, comparing with JOREK simulations,

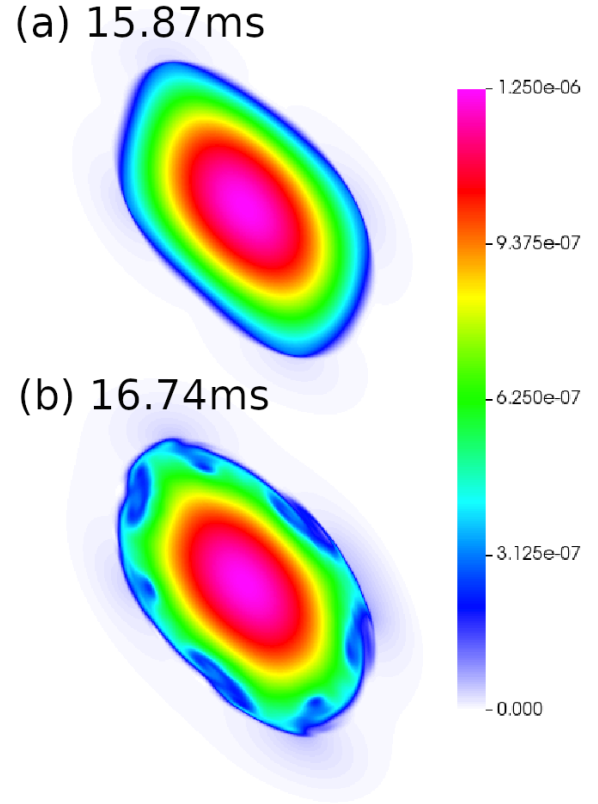


FIG. 21. Pseudocolour plots of temperature in JOREK normalised units at 15.87ms (top) and 16.74 ms (bottom). These time points are marked in Figure 20 (b) for the $N_p = 2$ stellarator case shown in Figure 20 (b). After the saturation of the initial (4, 1) kink mode, a (7, 2) mode structure develops later in time.

that the increase in the $n = 0$ magnetic energy observed in VMEC computations is due to an exchange of energy between the plasma and vacuum region. This explains the somewhat unintuitive result that the total energy within the plasma volume can sometimes increase once t preserving VMEC computations have converged to the nonlinearly saturated state.

By plotting the current distribution in JOREK, overlaid with Poincaré data, labelling field lines with the corresponding q value. It can be seen that the poloidal location of current sheets at the plasma boundary in VMEC and JOREK are consistent during the initial nonlinear saturation. Additional current sheets are observed later in JOREK solutions, and are expected to be omitted in VMEC, because they correspond to nonlinear interactions between competing modes, such as the (7, 2) mode, which are suppressed by the assumption of closed flux surfaces in the latter code. Both methods have numerical limitations in capturing these current sheets. Herein, it has been shown that VMEC can produce numerical current sheets if the resolution parameters are not appropriately chosen, and converged to sufficiently low force tolerances. Equally, the currents in JOREK can be more diffuse than an experimentally relevant result, due to the imposed classical resistivity at the plasma edge.

VMEC results can reproduce the qualitative trend in the saturated mode amplitude for both tokamak and stellarator cases, based on nonlinear analytic theory. However, there are stellarator cases which include higher Fourier harmonics, which deviate from this expected trend. These are considered to be bifurcated states of the initial equilibrium condition. JOEREK stellarator computations show that the saturated amplitude of the initial perturbation does decrease as a result of the increased external rotational transform.

This does not yet show that the MHD dynamics with increased t_{ext} are necessarily milder. Further into the nonlinear phase, all cases show signs of disruptive dynamics, as a (7, 2) island structure forms which begins to penetrate into the plasma column, leading to significant ergodisation. With increasing t_{ext} , the q profile flattens such that MHD modes can be expected to form broader structures. It is possible that the low shear allows MHD modes to overlap and ergodise the plasma column more easily in the tokamak case. The influence of the external rotational transform on the disruptive dynamics that are observed in JOEREK simulations will be the subject of future work.

The current work has relied on comparisons with linear growth rates, and other nonlinear simulation models to help constrain the VMEC solution space to results which are physically meaningful. Thus far, the author's work has focused on global conservation laws, and physical quantities, which has proven useful, but could be refined by enforcing constraints on the local structures observed. The formation of current sheets at the plasma boundary in Section II C is of particular interest. It has been demonstrated herein that local current sheets can be obtained which are broadly consistent with those observed in JOEREK nonlinear simulations. If the structure of the expected current sheets at the boundary can be known a priori, perhaps by comparing with linear theory, it may be possible to constrain the VMEC solutions further. The authors personally believe this a promising constraint to explore, and a dedicated comparison could be the subject of future work.

Beyond the application of constraints after VMEC computations have been converged, it would be interesting to see if the physical conservation laws and constraints could be enforced in VMEC during the computation itself. VMEC was after all not designed for the capture of nonlinearly saturated MHD perturbations. It could be possible that modifying the convergence algorithm could improve the physical validity of the solutions, without having to filter through the solution space manually, as has been done in this work. Such an endeavour has not been attempted thus far, to the author's knowledge.

Further work could also include additional physics studies, which apply the methods in this paper to consider several open advanced stellarator research questions. Low- n external modes observed on the W7-AS stellarator⁴¹, or external modes predicted in candidate quasi-axisymmetric stellarators⁴² could be considered. Such VMEC computations would help to gain an initial understanding of the nonlinear dynamics to help inform more detailed nonlinear studies with initial value codes, which could include non-ideal, and extended MHD effects. Of course, dedicated nonlinear studies

with initial value codes like JOEREK will also be important to interrogate such physics problems.

ACKNOWLEDGEMENTS

The authors would like to thank Florian Hindenlang, Ksenia Aleynikova, Nikita Nikulsin, Guillermo Suárez López, Michael Drevlak and Carolin Nuehnenberg for helpful discussions and assistance in the use of the codes used in this work.

Some of this work was carried out on the high performance computing architectures COBRA and RAVEN operated by MPCDF in Germany, JFRS-1 operated by IFERC-CSC in Japan, and the EUROfusion High Performance Computer (Marconi-Fusion).

This work has been supported in part by the Max-Planck/Princeton Center for Plasma Physics, and has been carried out within the framework of the EUROfusion Consortium, funded by the European Union via the Euratom Research and Training Programme (Grant Agreement No 101052200 — EUROfusion). Views and opinions expressed are however those of the author(s) only and do not necessarily reflect those of the European Union or the European Commission. Neither the European Union nor the European Commission can be held responsible for them.

REFERENCES

- ¹Weller A, Sakakibara S, Watanabe K, Toi K, Geiger J, Zarnstorff M, Hudson S, Reiman A, Werner A, Nührenberg C *et al.* 2006 *Fusion science and technology* **50** 158–170
- ²Zanini M, Buttenschön B, Laqua H, Thomsen H, Stange T, Brandt C, Braune H, Brunner K, Dinklage A, Gao Y *et al.* 2021 *Nuclear Fusion* **61** 116053
- ³Hirshman S P, van Rij W I and Merkel P 1986 *Comput. Phys. Commun.* **43** 143 URL [https://doi.org/10.1016/0010-4655\(86\)90058-5](https://doi.org/10.1016/0010-4655(86)90058-5)
- ⁴Turnbull A 2012 *Nuclear Fusion* **52** 054016
- ⁵Turnbull A, Ferraro N, Izzo V, Lazarus E A, Park J K, Cooper W, Hirshman S P, Lao L L, Lanctot M, Lazerson S *et al.* 2013 *Physics of Plasmas* **20** 056114
- ⁶Chapman I, Becoulet M, Bird T, Canik J, Ciansiosa M, Cooper W, Evans T, Ferraro N, Fuchs C, Gryaznevich M *et al.* 2014 *Nuclear Fusion* **54** 083006
- ⁷King J D, Strait E J, Lazerson S A, Ferraro N M, Logan N C, Haskey S R, Park J K, Hanson J M, Lanctot M J, Liu Y *et al.* 2015 *Physics of Plasmas* **22** 072501
- ⁸Cooper W, Graves J, Pochelon A, Sauter O and Villard L 2010 *Physical review letters* **105** 035003
- ⁹Graves J, Brunetti D, Chapman I, Cooper W, Reimerdes H, Halpern F, Pochelon A, Sauter O *et al.* 2012 *Plasma Physics and Controlled Fusion* **55** 014005
- ¹⁰Strumberger E, Günter S and Tichmann C 2014 *Nuclear Fusion* **54** 064019
- ¹¹Cooper W, Brunetti D, Duval B, Faustin J, Graves J, Kleiner A, Patten H, Pfefferlé D, Porte L, Raghunathan M *et al.* 2016 *Physics of Plasmas* **23** 040701
- ¹²Kleiner A, Graves J, Brunetti D, Cooper W A, Medvedev S, Merle A and Wahlberg C 2019 *Plasma Physics and Controlled Fusion* **61** 084005
- ¹³Brunetti D, Graves J, Cooper W A and Terranova D 2014 *Nuclear Fusion* **54** 064017
- ¹⁴Ramasamy R, Ramirez G B, Hoelzl M, Graves J, López G S, Lackner K, Günter S and Team J 2022 *Physics of Plasmas* **29** 072303
- ¹⁵Cooper W A, López-Bruna D, Ochando M A, Castejon F, Graves J, Kleiner A, Lanthaler S, Patten H, Raghunathan M, Faustin J *et al.* 2018 *Nuclear Fusion* **58** 124002

- ¹⁶Nikulsin N, Hoelzl M, Zocco A, Lackner K and Günter S 2019 *Physics of Plasmas* **26** 102109
- ¹⁷Zhou Y, Ferraro N, Jardin S C and Strauss H R 2021 *Nuclear Fusion* **61** 086015
- ¹⁸Garabedian P R 2006 *Proceedings of the National Academy of Sciences* **103** 19232–19236
- ¹⁹Suárez L *et al.* 2020 *Effect of non-axisymmetric tokamak plasmas on the coupling performance of ion cyclotron wave antennas* Ph.D. thesis
- ²⁰Lazerson S A, Loizu J, Hirshman S and Hudson S R 2016 *Physics of Plasmas* **23** 012507
- ²¹Hoelzl M, Huijsmans G, Pamela S, Becoulet M, Nardon E, Artola F J, Nkonga B, Atanasiu C, Bandaru V, Bhole A *et al.* 2021 *Nuclear Fusion* **61** 065001
- ²²Nikulsin N, Ramasamy R, Hoelzl M, Hindenlang F, Strumberger E, Lackner K, Günter S and Team J 2022 *Physics of Plasmas* **29** 063901
- ²³Arber T, Longbottom A and Van der Linden R 1999 *The Astrophysical Journal* **517** 990
- ²⁴Kadomtsev B and Pogutse O 1973 *Sov. Phys. JETP* **5** 575–590
- ²⁵Hirshman S P and Whitson J 1983 *The Physics of fluids* **26** 3553–3568
- ²⁶López G S, Ochoukov R, Tierens W, Willensdorfer M, Zohm H, Aguiam D, Birkenmeier G, Bobkov V, Cavedon M, Dunne M *et al.* 2019 *Plasma Physics and Controlled Fusion* **61** 125019
- ²⁷Shafranov V and Zakharov L 1972 *Nuclear Fusion* **12** 599
- ²⁸Drevlak M, Monticello D and Reiman A 2005 *Nuclear fusion* **45** 731
- ²⁹Merkel P 1987 *Nuclear Fusion* **27** 867
- ³⁰Wesson J 1978 *Nuclear Fusion* **18** 87
- ³¹Strumberger E and Günter S 2017 *Nuclear Fusion* **57** 016032
- ³²Kleiner A, Graves J, Cooper W, Nicolas T and Wahlberg C 2018 *Nuclear Fusion* **58** 074001
- ³³López G S, Ciansiosa M, Lunt T, Tierens W, Bilato R, Birkenmeier G, Bobkov V, Dunne M, Ochoukov R, Strumberger E *et al.* 2020 *Plasma Physics and Controlled Fusion* **62** 125021
- ³⁴Lionello R, Velli M, Einaudi G and Mikić Z 1998 *The Astrophysical Journal* **494** 840
- ³⁵Kliem B, Titov V and Török T 2004 *Astronomy & Astrophysics* **413** L23–L26
- ³⁶Huang Y M, Hudson S R, Loizu J, Zhou Y and Bhattacharjee A 2022 *Physics of Plasmas* **29** 032513
- ³⁷Eriksson H and Wahlberg C 1997 *Plasma physics and controlled fusion* **39** 943
- ³⁸Artola F J, Beyer P, Huijsmans G, Loarte A and Hoelzl M 2018 *Free-boundary simulations of MHD plasma instabilities in tokamaks* Ph.D. thesis Aix-Marseille Université URL <https://hal-amu.archives-ouvertes.fr/tel-02012234v1>
- ³⁹Ramasamy R 2022 *Equilibrium and initial value problem simulation studies of nonlinear magnetohydrodynamics in stellarators* Ph.D. thesis
- ⁴⁰Hindenlang F, Maj O, Strumberger E, Rampp M and Sonnendrücker E 2019 GVEC: A newly developed 3D ideal MHD Galerkin Variational Equilibrium Code Presentation given in 2019Simons Collaboration on Hidden Symmetries and Fusion Energy2019 URL <https://hiddensymmetries.princeton.edu/meetings/simons-hour-video-talk>
- ⁴¹Merkel P, Nuehrenberg C and Cooper W 1996
- ⁴²Strumberger E and Günter S 2019 *Nuclear Fusion* **59** 106008